Regional Stratigraphy of the South Polar Layered Deposits (Promethei Lingula, Mars): "Discontinuity-bounded" Units in Images and Radargrams

Luca Guallini[1,2] (luca.guallini@space.unibe.ch)
Angelo Pio Rossi[3,4] (an.rossi@jacobs-university.de)
François Forget[5] (forget@lmd.jussieu.fr)
Lucia Marinangeli[2] (lucia.marinangeli@unich.it)
Sebastian Emanuel Lauro[6] (lauro@fis.uniroma3.it)
Elena Pettinelli[6] (pettinelli@fis.uniroma3.it)
Roberto Seu[7] (robseu@infocom.uniroma1.it)
Nicolas Thomas[1] (nicolas.thomas@space.unibe.ch)

[1]Space Research and Planetary Sciences, Physics Institute
University of Bern, Switzerland

[2]Laboratorio di Telerilevamento e Planetologia
Dipartimento di Scienze Psicologiche, della Salute e del Territorio
Università d'Annunzio
Via dei Vestini, 31
66100 Chieti Scalo, Italy

[3]Jacobs University Bremen
Campus Ring 1
28759 Bremen, Germany

[4]International Space Science Institute

Hallerstrasse 6
3012 Bern, Switzerland

[5]LMD, Institut Pierre Simon Laplace
Université Paris 6
BP 99, 4 place Jussieu,
75005 Paris, France

[6]Dipartimento di Matematica e Fisica
Università di Roma Tre
Via della Vasca Navale, 84
00146 Roma, Italy

[7]Dipartimento di Scienza e Tecnica dell'Informazione e Comunicazione
Università La Sapienza
Via Eudossiana, 18
00184 Roma, Italy

Corresponding Author:
Luca Guallini
Space Research and Planetary Sciences, Physics Institute
University of Bern, Switzerland
Sidlerstrasse, 5, CH-3012, Bern, Switzerland
Phone: +41 31 631 80 45
e-mail: luca.guallini@space.unibe.ch

Highlights

- We defined a new regional stratigraphy of the SPLD in Promethei Lingula;

- The stratigraphic units are defined on the basis of defined discontinuities;

- The discontinuities have been mapped both in images and radargrams;

- The regional stratigraphy suggests climate and orbital changes on Mars in the past.

Abstract

The Mars South Polar Layered Deposits (SPLD) are the result of depositional and erosional events, which are marked by different stratigraphic sequences and erosional surfaces. To unambiguously define the stratigraphic units at regional scale, we mapped the SPLD on the basis of observed discontinuities (i.e., unconformities, correlative discontinuities and conformities), as commonly done in terrestrial modern stratigraphy. This methodology is defined as "Discontinuity-Bounded Units" or allostratigraphy, and is complemented by geomorphological mapping.

Our study focuses on Promethei Lingula (PL) and uses both high-resolution images (CTX, HiRISE) and radargrams (SHARAD) to combine surface and sub-surface observations and obtain a 3D geological reconstruction of the SPLD. One regional discontinuity (named AUR1) was defined within the studied stratigraphic succession and is exposed in several non-contiguous outcrops around PL as well as observed at depth within the ice sheet. This is the primary contact between two major depositional sequences, showing a different texture at CTX resolution. The lower sequence is characterized mainly by a "ridge and trough" morphology (Ridge and Trough Sequence; RTS) and the upper sequence shows mainly by a "stair-stepped" morphology (Stair-Stepped Sequence; SSS). On the basis of the observations, we defined two regional "discontinuity-bounded" units in PL, respectively coinciding with RTS and SSS sequences. Our stratigraphic reconstruction provides new hints on the major scale events that shaped this region. Oscillations in Martian axial obliquity could have controlled local climate conditions in the past, affecting the PL geological record.

Keywords

Geological processes

Mars, polar geology

Mars, surface

Image processing

1. Introduction

The Amazonian South Polar Layered Deposits (SPLD) [e.g., *Herkenhoff and Plaut*, 2000; *Koutnik et al.* 2002] cover most of Planum Australe [*Tanaka and Scott*, 1987] and consist of a up to ~3.7 kilometer-thick stratified sequence (Apl Unit; *Tanaka and Kolb* [2001]; *Kolb and Tanaka* [2001]). Their inferred composition of water ice with minor impurities [e.g., *Cutts*, 1973; *Kieffer et al.*, 1976; *Thomas et al.*, 1992; *Mellon*, 1996; *Clifford et al.*, 2000] has been indirectly verified by Martian subsurface radar sounders [*Nunes and Phillips*, 2006; *Plaut et al.*, 2007] and by density considerations derived from analysis of gravity anomalies associated with Planum Australe [*Zuber et al.*, 2007; *Wieczorek*, 2008; *Li et al.*, 2012]. Both sets of studies estimate upper limits of the volume fraction of sediments of 10%-15%. Subsurface deposit of CO_2 ice [*Phillips et al.*, 2011] and possibly of CO_2 clathrate hydrates (e.g., *Kolb and Tanaka* [2000], *Kargel and Tanaka* [2002], *Wieczorek* [2008]) was hypothesized in the SPLD. Compositional variations have been also suggested by the structural and rheological analysis of deformational systems observed within the SPLD in the PL region, which is again consistent with potentially interbedded layers of CO_2 or CO_2 clathrate hydrates [*Guallini et al.*, 2012].

The inner, thickest portion of the SPLD reaches ~3-4 km in thickness [*Plaut et al.*, 2007; *Byrne*, 2009]. The layered deposits decrease in elevation and thickness toward the ice-dome margins, where lower-relief plateaus are located (i.e., lingulae or lobes). These plateaus (i.e., Australe Lingula (AL), Promethei Lingula (PL) and Ultima Lingula (UL)) are dissected and separated by the recent development of reentrant canyons (e.g. Promethei Chasma (PC), Ultima Chasma (UC) and Chasma Australe (CA); [*Byrne and Ivanov*, 2004]), which are hypothesized to have been formed by katabatic wind scouring and ablation [e.g., *Kolb and Tanaka*, 2001; *Tanaka et al.*, 2008; *Warner and Farmer*, 2008] or by catastrophic outflow of meltwater (jökulhlaup-like discharges; e.g., *Clifford* [1987]; *Anguita et al.* [2000]).

Several authors have used images and radargrams to study the regional SPLD stratigraphy and have described major stratigraphic successions that define distinct units [e.g., *Byrne and Ivanov*, 2004; *Kolb and Tanaka*, 2001, 2006; *Milkovich and Plaut*, 2008]. As concluded in previous studies, the overall depositional history of the SPLD, especially along their margins, has been irregular in time and space. In particular, like in the North Polar Layered Deposits (NPLD), stratigraphic unconformities between the SPLD sequences are locally exposed (i.e. irregularly distributed), suggesting a discontinuous depositional record over time [*Malin and Edgett*, 2001; *Kolb and Tanaka*, 2006; *Seu et al.*, 2007; *Milkovich and Plaut*, 2008; *Milkovich et al.*, 2009; *Guallini et al.*, 2010]. The unconformities, together with the variable ice and dust contents of different layers, are considered to represent past climatic variations [e.g., *Toon et al.*, 1980], occurred in response to significant quasi-periodic changes in the Martian orbital parameters [*Cutts and Lewis*, 1982; *Thomas et al.*, 1992], similar to terrestrial Milanković cycles. In particular, spectral analyses of the PLD with depth (mainly of the NPLD; e.g., *Milkovich and Head* [2005]) are based on *Laskar et al.* [2002] and agrees with the glacial and interglacial ages reconstructed by *Head et al.* [2003]. However, this methodology is still debated because necessitate major assumptions and hypotheses [e.g., *Perron and Huybers*, 2009], especially regarding the SPLD.

This work focuses on a new definition of the regional stratigraphy of PL (Fig. 1a-c; latitude ~70°-80° S; longitude ~90°-160° E). The study site has been chosen because 1) it consists of well exposed and laterally continuous SPLD sequences; 2) there is a good dataset coverage. According to MARSIS radar data analyzed by *Plaut et al.* [2007], the present-day thickness of the SPLD sequence in PL (which overlaps the Noachian and Hesperian bedrock units [*Kolb and Tanaka*, 2006]) is comprised between ~500 and ~2500 m (± 200 m of vertical uncertainty).

1.2 Background

1.2.1 Definition of the stratigraphic units

The limits of remote sensing analysis, the absence (or undiscovered presence) of fossils on Mars, the icy bulk composition of the SPLD (i.e., they are not rocks in the strict sense) and the poor constraints of their physical and chemical properties prevent the use of most of the usual terrestrial stratigraphic methodologies (e.g., lithostratigraphy, biostratigraphy, etc.) to understand the stratigraphy of the SPLD. On the other hand, stratigraphic reconstructions based on observable surface texture, erosional style and brightness of the sequences have been previously attempted [e.g., *Byrne and Ivanov*, 2004; *Milkovich and Plaut*, 2008]. However, this approach can be affected by incorrect interpretations or uncertainties due to potential similarities between different layers in different sequences, to variations in local topography (surface slope and orientation), to diverse illumination conditions, to the presence of dust mantling or seasonal frost, to the use of visible images with different resolution, to the scale of observation, and to the considered layers properties [e.g., *Herkenhoff and Murray*, 1990; *Herkenhoff et al.*, 2007; *Fishbaugh et al.*, 2008; *Fishbaugh et al.*, 2010]. All these elements, in general, have a significant influence on the appearance of the layers in terms of brightness and texture [*Milkovich and Plaut,* 2008] and hide their real bulk properties, often precluding the possibility of correlation among different sections.

In addition to optical images, subsurface radar instruments have been previously used as complement to outcrop-based studies. In particular, radargrams have been analyzed to identify interfaces (i.e. the internal stratigraphy) within the SPLD [e.g., *Milkovich and Plaut*, 2008], overcoming the limitations of visible exposures. However, radar reflectors may not be always mapped or associated with real subsurface layering. In fact, bad correlations can be due to subsurface off-nadir reflections (i.e., clutter) or multiple reflections [e.g., *Nunes and Phillips*, 2006; *Plaut et al.*, 2007; *Christian et al.*, 2013], to conductivity/density variations at depth [e.g., *Reeh et al.*, 1991; *Dowdeswell and Evans*, 2004] and to the different resolution of the dataset [*Nunes and Phillips*, 2006; *Fishbaugh et al.*, 2008; *Christian et al.*, 2013]. Furthermore, and on the contrary than on the Earth, where it is possible to interpolate other kinds of measurements from ice cores [*Eisen et al.*, 2003], correlation between radar and visible layering on Mars it is complicated: 1) By the absence of unambiguous constraints about the SPLD stratigraphy, chemistry and dust distribution [*Milkovich et al.*, 2009]; 2) Because it is currently unknown what causes reflectors exactly [e.g., *Lalich and Holt*, 2016]. Finally, in several cases, SPLD radargrams are also characterized by wide no-signal zones defined as "Reflection Free Zones" [*Phillips et al.*, 2011], which may be caused by successions of layers with low dielectric contrast [*Grima et al.*, 2011].

1.2.2. Study aims

To try to avoid all the problematics related to the previous considerations, the present study relates to the "discontinuity-bounded" classification or "allostratigraphy" [*Chang*, 1975; *Salvador*, 1987] principles. Units are defined making use of surfaces (instead of strata) interrupting the continuity of the sequences of layers and recording events that interrupted the deposition. In fact, according to the conventional stratigraphy on Earth [*Salvador*, 1987]:

1) Discontinuities mark a stratigraphic contact [e.g., *Bates and Jackson*, 1987] and can be used to designate a stratigraphic unit (i.e., a mappable body of rock) [*Sloss et al.*, 1949; *Catuneanu*, 2006];

2) Discontinuities divide the geologic record into genetically related packages of strata (units) and can be used for stratigraphic correlation [e.g., *Sloss*, 1963; *Wheeler*, 1964; *Catuneanu*, 2006].

These discontinuities are mappable lithological contacts with or without a stratigraphic hiatus or erosion [*Catuneanu*, 2006], thus including both unconformities and conformities [*Mitchum*, 1977]. The definition of the discontinuity-bounded sequences is irrespective of their eventual morphological or lithological lateral changes in the depositional environment [Catuneanu, 2006].

Based on above mentioned principles, the use of discontinuities can minimize most of the ambiguities derived from the lonely use of the morphologic aspect of the SPLD sequences and of marker layers [e.g., *Byrne and Ivanov*, 2004; *Milkovich and Plaut*, 2008]. In particular, we used observed or inferred stratigraphic discontinuities (both along the marginal scarps and in the subsurface of PL) to define the regional stratigraphy of the SPLD. In fact, it is well known that the SPLD are characterized by discontinuities: *Kolb and Tanaka* [2006] first reported angular unconformities in PL using Thermal Emission Imaging System (THEMIS) visible images [*Christensen et al.*, 2004]. At the same time, buried unconformities have been observed in radargrams [*Seu et al.*, 2007; *Milkovich et al.* 2009].

Unconformities are important markers of the deposition/erosion of the Polar Layered Deposits in both hemispheres, in turn related to global or regional climate changes [*Fishbaugh et al.*, 2008]. Such climate changes are thought to have been induced by variations in Mars orbital parameters, especially its spin axis obliquity [*Levrard et al.*, 2007; *Greve et al.*, 2010; *Forget et al.*, 2017 in press]. Even if we can only speculate about the variations of the mean obliquity at the time of the formation of the SPLD [*Laskar et al.*, 2004], studying the unique SPLD stratigraphy using discontinuities might enable us to constrain the obliquity history of Mars and to refine the understating of climate changes during the Late Amazonian.

1.2.3. Used terminology and definitions

The “discontinuity-bounded” classification assumes that:

1) A "conformity" is a true discontinuity that marks no interruption in the sequence of beds;
2) An “unconformity” is a true discontinuity that marks interruption in the sequence of beds.
3) Within the same sedimentary environment, each unconformity can be correlated in continuity (or not) with the laterally equivalent correlative conformity [*Mitchum*, 1977; *Posamentier et al.*, 1988; *Van Wagoner*, 1995]. This technique is commonly used on Earth: through these surfaces, the sequence boundaries can be extended from the observed unconformities across an entire sedimentary environment, allowing the construction of cross sections and thus of the regional stratigraphy of a sedimentary body [*Catuneanu*, 2006].

On the basis of the above-mentioned principles, in the present paper we refer to:

1) An “angular unconformity” (AU) when there is an observable unconformity (commonly an erosional surface showing abrupt layers truncation) between two rock sequences whose bedding planes are not parallel [*Bates and Jackson*, 1987]. We follow the established practice in planetary remote mapping of using the definition of angular unconformity independently of the geological factors causing the inclination of the SPLD layers;

2) A "correlative discontinuity" (CD) when it is possible to correlate one or more observed angular unconformities bounding the same sequence(s) across a broad region (i.e. same depositional basin) [*Mitchum*, 1977]. It is assumed that a) the correlative discontinuity is located in the same elevation range of the observed angular unconformities, b) the correlative discontinuity and the angular unconformities formed under the same controlling factors [*Mitchum*, 1977; *Catuneanu*, 2006]. Thus, the correlative discontinuity is mapped in lateral continuity with the local angular unconformities, following the inferred stratigraphic position of the angular unconformity.

3) A "correlative conformity" (CC) when it is possible to correlate one or more observed angular unconformities bounding the same sequence(s) across a broad region (i.e. same depositional basin) [*Mitchum*, 1977] but not in lateral continuity with the angular unconformities. It is assumed that the correlative conformity a) can be affected or not by erosion or a depositional hiatus (the use of correlative continuities is irrespective of the nature of the surface itself [e.g., *Catuneanu*, 2006]), b) is in the same elevation range of the mapped angular unconformities. In other words, the angular unconformities and correlative conformities with the same elevation range and separating the same sequences can be correlated [*Catuneanu*, 2006].

4) A "discontinuity" (Dis) when we generically speak of a stratigraphic contact between two sequences.

For simplicity and clarity, independent of their nature, all bounding surfaces that can be regionally correlated (through conformities and discontinuities) with exposed angular unconformities (AU) and inferred to have been formed under the same controlling factors are named "AURn", where "R" stands for regional and "n" is a chronological number that is a function of the stratigraphic position of the regional discontinuity.

1.2.4. Dataset

The region has been analyzed using high-resolution images derived from the Context camera (CTX, 6.0 m/pix; *Malin et al.* [2007]) and the High Resolution Imaging Science Experiment camera

(HiRISE, 0.25-0.32 m/pix; *McEwen et al.* [2007]), both onboard the NASA Mars Reconnaissance Orbiter (MRO). Although the studied images (approximately one hundred) do not completely cover the PL area, the spatial resolution of the dataset is sufficient to resolve the structures in detail. In particular, the high resolution of the CTX and HiRISE images allow us to better exclude false angular unconformities due to optical effects (i.e., apparent angles) [*Fishbaugh et al.*, 2008] or created by complex topography (e.g., slope breaks within the sequence, scarps crosscutting layers, etc.). In some cases, when CTX and HiRISE data were not available, Mars Express High Resolution Stereo Camera (HRSC) Level-3 (nd3) images (nadir channel, 12.5, 25.0 and 50 m/pix of spatial resolution) were used [*Neukum et al.*, 2004; *Gwinner et al.*, 2010].

The topographic base map was obtained from the Mars Orbiter Laser Altimeter (MOLA) Digital Elevation Model (DEM) sampled on a 512 pix/degree grid, equivalent to a spatial resolution of ~115 m at polar latitudes [*Smith et al.*, 2001].

The optical and topographic dataset was processed using the USGS Integrated Software for Imager and Spectrometers (ISIS 3) and analyzed using ESRI ArcGIS. Raster images were draped onto MOLA Digital Terrain Model using ESRI ArcScene to obtain three-dimensional views. Images were processed in a polar stereographic projection. For each image, coordinates are given in decimal degrees (longitude domain -180°/180°, positive east). When possible, only images acquired during Ls ~230°-260° (southern late spring), Ls ~270°-350° (southern summer) and Ls ~0°-30° (southern early autumn) were selected because of the absence or reduction of CO_2 ice, which condenses on the surface of the layers during the cold seasons.

The interior of the SPLD has been analyzed using Italian RDR SHARAD data [*Seu et al.*, 2007], converted to raster format and manually mapping reflectors/bounding surfaces using graphical programs. In total, about 600 radargrams have been analyzed. The sounding radar operates at a central frequency of 20 MHz (10 MHz of bandwidth) and has a theoretical vertical resolution of ~15 m in free space [*Seu et al.*, 2007; *Plaut et al.*, 2007] (~10 to 20 m in PLD [e.g. *Nunes*, 2006; *Nunes*, 2011; *Lalich and Holt*, 2016), an along-track resolution of approximately 0.3 -

1.0 km and a cross-track resolution of approximately 3 - 6 km.

We selected representative profiles for the analysis (Fig. 1a). In the radargrams, the vertical axis represents the two-way travel time in microseconds and is converted to depth using a dielectric constant of 3.4, which is consistent with a mixture of 90% water ice and 10% basaltic impurities [e.g. *Heggy et al.*, 2007; *Plaut et al.,* 2007; *Seu et al.,* 2007]. This value is used only below the reflection corresponding to the SPLD surface.

As previously cited, the interpretation of the reflectors in the SPLD are often uncertain because of strong surface/subsurface clutter. Thus, used radar tracks were simulated using algorithms developed by the Italian SHARAD team to identify the most important clutter [e.g., *Russo et al.*, 2008].

2. Results

2.1. Description of the discontinuities in images

On the basis of the areal coverage of the images dataset, several stratigraphic sections (or logs; L1-L21 in Fig. 1a and Table 1) of interest have been identified along the walls of marginal erosional scarps of PL and of the chasmata, troughs and reentrants.

Some exposures clearly show sequences interrupted by angular unconformities (see Fig. 1a for location), which can in turn be correlated with correlative discontinuities or conformities. The angular unconformities (cf. Figs. 2-4 and A1-A3) are located in the SPLD sequence between a minimum of ~1400 m and a maximum of ~2500 m (average of ~1800-1900 m) in MOLA height. In most of the cases, these bounding surfaces confine sequences having similar appearance. In general, the elevations and the lengths of the angular unconformities (which are in some cases traceable over tens of kilometers; Fig. 1a) are comparable to those observed for angular unconformities in other locations of the Planum Australe ice dome [e.g., *Kolb and Tanaka*, 2006; *Milkovich and Plaut*, 2008].

By applying the geologic V-rule [*Simpson*, 1968; *Meentemeyer and Moody*, 2000] and studying the geometric relationships in plan view between the topographic surface (marked by the elevation contours) and the locally exposed contour planes of the discontinuities (deduced by their mapped plan-view traces), we noticed that these contour planes are generally curved lineaments conformable with topographic contours (i.e., they have the same bending polarity). This geometric arrangement entails planes dipping in the same direction as the slope (i.e., toward the SPLD margins), but with a shallower dip angle (in general, < 1°).

Most representative cases are located in three regions:

1) In the first location (Figs. 1a and 2; L7b in Tab. 1) the stratigraphic exposure shows an angular unconformity located along the PL margin at an average elevation of about 1800 m. The AU can be followed with quasi-continuity for about 120 km and correlated with correlative discontinuity/conformity (L7a, c in Tab. 1). The AU separates two distinct morphologic sequences.

2) The second angular unconformity (Fig. 3) is exposed along Ultimum Chasma scarps (L18; cf. Tab. 1) at an average elevation of about 1850 m. The AU can be correlated with a correlative discontinuity and mapped for about 90 km. It divides two morphologic sequences similar to those observed in L7.

3) Another stratigraphic outcrop showing an angular unconformity is exposed in Promethei Chasma scarps (L20; Fig. 4 and Tab. 1). The AU is located at an average elevation of about 2150 m and can be correlated with correlative discontinuity for about 60 km. It bounds two morphologic sequences again similar to those observed in L7 and L18.

2.2. Description of the discontinuities in radargrams

Angular unconformities can also be identified in some radargrams (tracks from 1 to 27 in Fig. 1a), where the observed reflectors seem to be locally inclined and truncated. In particular, at different levels of confidence, we observed potential radar unconformities in 28 locations (cf. Table 2). The unconformable surfaces are sub-horizontal, laterally extend up to approximately 100 km on average and are primarily focused in one broad area of PL (cf. white dotted inset in Fig. 1a), plus other minor and more uncertain regions.

The main area characterized by the presence of radar angular unconformities is located in the middle of the PL, equatorward of the Australi Sulci and poleward of the visible sections L7, L9 and L10 (where angular unconformities are exposed; 80°S-85°S latitude; 110°E-130°E longitude; Fig. 1a; (1) in Table 2). With respect to the maximum length of the PL ice sheet, several longitudinal radar profiles (Figs. 5, 6, A4 and A5) display two packs of reflectors with a different dip-angle. In particular, some of the reflectors (usually the bottom ones) seem to be truncated against others (usually the top ones) that are continuous, sub-parallel and with a dip toward the PLD margins. The angle between the two sets of reflectors suggests an unconformable contact between two radar sequences. This observation is consistent with *Seu et al.* [2007] and *Milkovich et al.* [2009]. The observed angular unconformities are located at average elevations of ~1900 m. The same structural configuration – even if subtler – can be detected in data from transverse orbits (e.g., Figs. 7 and A6) that crosscut the longitudinal orbits. This evidence supports the idea that the observed angular unconformities are real geologic structures, as previously suggested by some authors (e.g., *Seu et al.* [2007]). The high number of crosscutting radar tracks covering the study area allows us to interpolate the minimum, intermediate and maximum points of elevation (in terms of latitude, longitude and depth below the topographic surface) of the angular unconformities observed in each 2D single orbit to obtain a three-dimensional view of the buried unconformable surface (Fig. 8). The interpolation of sample elevation points has been automatically calculated by using ArcGIS, adopting Kriging method. This kind of interpolation is a geostatistical technique often used on soils science and geology, that on the contrary of other tools minimizes the mean square error [e.g., *Burrough*, 1986; *Oliver*, 1990]. In this location, the reconstructed buried 3D angular unconformity is a continuous rough surface with an approximate area of 10,000 km^2 and a slight dip toward the SE (~0.04°-0.6° dip angle). Its average elevation and dipping direction makes the observed angular unconformity consistent with the unconformities defined in the visible images.

The second location is in the same latitude range as the previous one (80°S-85°S) but between the longitudes of 100°E and 110°E (17, 25, 28 in Fig. 1a; cf. Fig. 9 and location (2) in Table 2). Two sets of intersecting radargrams show again two groups of (less bright) reflectors that have different dip angles and appear to be truncated, thus suggesting the presence of an angular unconformity between them. This latter surface dips toward the PL margins (i.e., to the east) at a low angle (~0.1-0.2°). If the angular unconformity plane were to extend to the PL margin, it would intersect the topographic surface corresponding to the L7 section at an elevation of approximately 2000 m. This value is again consistent with the local elevation of the angular unconformities observed in the images.

2.3. Description of the stratigraphic sequences in the visible images

As aforesaid, the observed discontinuities divide two main stratigraphic sequences within the SPLD. These sequences, which most important distinguishing features are highlighted in Figures 10-12, differ in average layer thickness, in morphology, in brightness and in erosional behavior of the bedding planes. The transition between the two sequences is, in some cases, marked by a slight break in topographic slope (cf. Fig. 13 as an example) that corresponds to the topographic contour of the discontinuities. In particular, the basal sequence is characterized by a higher dip angle of the scarp (~5° to 20°) than the top sequence (~1° to 10°).

2.3.1. Ridge and Trough sequence (RTS)

The basal sequence resting below the discontinuities is mainly characterized by a “ridge and trough" morphology, firstly defined by *Malin and Edgett* [2001] (Figs. 10, 11). On average, the package of layers is approximately 650-700 m thick. The RTS shows lateral variations in thickness and textures that may be due to different erosion or deposition rates (cf. Fig. A3a and layer S15 in Fig. A7).

The sequence is mostly characterized by irregularly alternating dark and bright layers that are generally thin (up to some meters in thickness; Fig. 11a). From their appearance, these layers can be grouped into stratigraphic packs that are clearly distinguishable from adjacent ones (cf. Figs. A7-A9). In some cases, a further minor-order layering of sub-meter thickness appears at a closer scale (HiRISE resolution; cf. Fig. 11b).

By considering the direction of illumination of the scarp in the images and from HiRISE DTM (cf. Fig. 14 in *Guallini et al.* [2012]), we observed that dark bedding planes generally show a typical concave-upward profile ("trough-shaped" morphology; Tr in Fig. 11b) while bright layers have a convex-upward profile ("ridge-shaped" morphology; Rg in Fig. 11b) [*Malin and Edgett*, 2001]. Thus, the brightness might vary consistently with the morphology and texture of the layers and could be influenced by the dust content of their bulk composition [e.g., *Squyres*, 1979; *Jakosky et al.*, 1995; *Malin and Edgett*, 2001; *Richardson and Wilson*, 2002; *Haberle et al.*, 2003; *Mischna et al.*, 2003; *Milkovich and Head*, 2005]. In this case, the higher absorption of the solar radiation in the dark layers, causing their high rate of sublimation (i.e., the relative velocity at which the icy matrix sublimates), could explain their "trough-shaped" morphology. Vice-versa, the opposite reasoning can be made for bright layers. On the other hand, another (in our advice) less possible hypothesis is that "trough-shaped" layers appear darker than the "ridge-shaped" ones because dust deposited more easily on their hollowed surface. In this last case, the variation of brightness of the layers would be only apparent and not representative of their bulk composition.

At CTX resolution, the surfaces of the bedding planes appear uneven and locally pitted (Fig. 11b, c). This erosional texture varies in intensity from layer to layer and whereas, again, it was indicative of the real bulk composition of the bedding planes, could change as a function of the varying mechanical strengths to erosion and the varying rates of sublimation of the layers. In addition, jagged layer edges (Ne in Fig. 11a) are not uncommonly observed in plan view. They have an almost regular pattern that may indicate a pristine structural control (preferential pathways of fracturing) on their erosion [*Guallini et al.*, 2012].

The vertical variation of layer thickness along the RTS sequence appears to be irregular (as observed by *Limaye et al.* [2012] at other SPLD sites). Thus, a specific thickening gradation is not clearly identifiable.

The RTS sequence is occasionally interrupted by single or limited groups of “bench-like” bedding planes, typically of sub-decameter thickness (Bn in Fig. 11). These layers, which are prevalent in the upper sequence, are characterized by an irregular erosional pattern on their surfaces and by notched edges, which are sometimes clearly marked. They are locally more common in topographically higher observed outcrops.

2.3.2. Stair-Stepped sequence (SSS)

The sequence resting upon the discontinuities is characterized by a “stair-stepped" morphology [*Malin and Edgett*, 2001], marked by a regular and clear bench-like morphology (Figs. 10, 12). The sequence has a maximum thickness of ~700 m, but this may be an underestimate because the elevation of its basal surface is uncertain in some places.

In general, the layers and layer packs are up to decametric in thickness and lack significant brightness variations. They mostly appear medium-dark toned, possibly because of dust mantling. The surfaces of the layers generally show an uneven and pitted erosional pattern (see layer surfaces in Fig. 12). However, it is not clear if this texture is linked to an inner property of the bulk composition of the bedding planes or to the overlying dust deposit. The edges of these strata are often notched (Ne in Fig. 12).

In addition to the dominant “stair-stepped” characteristic of the sequence, several variations in stratigraphy are present. For example, some SSS outcrops show a “ridge and trough” morphology in some layer packs in Chasma Australe, which is more similar to the RTS (see L18-L20 in Figs. 3-4 and Fig. 14). The “ridge and trough” sub-sequences are mainly exposed toward the base of the SSS sequence, close to the discontinuity surfaces, which may suggest a local progressive transition from the RTS.

2.3.3. Minor-order morphostratigraphic sequences

Within the major-order stratigraphic sequences (i.e., RTS and SSS), it is possible to observe several minor-order "morpho-sequences" in layer blocks showing similar morphologies and possible vertical repetition along the exposure (cfr. Fig. A10 and Tables A1-A3). The differences between these possible minor-order sequences are in terms of number of layers, stratigraphic location and texture. In addition, in most cases, sub-sequences present in one exposure are completely absent in others: they lack regional continuity, as occasional exposure of lateral pinch-out terminations of the layers also suggests (cf. S15 and Fig. A7). It follows that, within the RTS and SSS sequences, each analyzed outcrop shows minor-order packs of layers that can be correlated across the PL only with difficulty, which may outline local independent events superimposed on regional ones. However, according to the stated stratigraphic approach, although the presence of minor-order sequences certainly implies greater complexity in the SPLD stratigraphy, we chose to limit our analysis to the regional events.

2.4. Brief description of the stratigraphic sequences in radargrams

Based on observation of the unconformities in the radargrams, two SPLD radar sequences that occasionally intersect the PL topographic surface can be defined. The transition between the two sequences is in some cases marked by low intensity reflections zones ~100 m thick that rests upon the unconformities when present (letter A in Figs. 5, 6 for location).

Although the appearance of the two bounded sequences is generally very similar when examined at radar wavelengths, at the PL margins it is possible to observe some variations: 1) the upper sequence is thinner than the bottom one; 2) the reflectors of the two radar sequences both dip slightly toward the PL margins but have different (apparent, due to view geometry) dip angles (~1.5° upper sequence vs. ~0.1° bottom sequence; cf. Fig. 6 for example); and 3) reflectors are lower in number or locally absent in the top portion of the upper sequence. All these elements agree with the observations in the visible images and the two radar sequences seem to represent the same stratigraphy of the RTS and SSS.

3. Discussion

3.1. Definition of the regional discontinuity "AUR1"

The observed unconformable surfaces are not continuously exposed across the PL margins. This implies some uncertainties in their stratigraphic positions and thus their correlation. On the other hand, their exposure in various places suggests their presence at regional scale in PL. Also, despite the elevation of the exposed unconformities is not constant from section to section (it generally decreases toward the PL margins), at the regional scale several do not show significant variations in topographic heights (comprised between ~1900 ± 100 m in average; Fig. 15 and Tab.1).

All these angular unconformities divide the RTS and SSS sequences. Around the PL margins and also along the scarps of PC, UC and CA, these unconformities can be correlated through correlative discontinuities and conformities (the most significant examples are reported in Figs. 2, 4, 5). We speculate that these unconformities originated under the same erosional or non-depositional event. As a result, we assume that all these local discontinuities (unconformable and conformable) can be related to one regional discontinuity surface, appointed as AUR1 (Figs. 2-5 and Tab. 1).

The local differences in elevation of the unconformities can be explained as following:

1) They are a unique and continuous surface but the erosion rate could have varied spatially in PL as a function of the existing local factors (i.e., narrow-scale topography, layer consistency, etc.) and resulted in both unconformable and conformable surfaces. As instance, it is possible that, in some locations, depositional lag formed in place of the angular unconformities [e.g., *Fishbaugh et al.*, 2008; *Byrne*, 2009].

2) They are a unique and almost continuous regional surface that is topographically irregular. Assuming this case, it is possible to calculate that the regional surface plane has a gentle slope of ~0.05° along the NS sections and ~0.1° along the EW sections (cf. Fig. 1a), dipping toward the PL margins. This attitude is consistent with that derived from the radargrams (cf. Section 2.2). It is also

consistent with *Byrne and Ivanov* [2004], calculating a slight dip angle of the SPLD toward the periphery of the ice dome, progressively flattening toward its margins. In this sense, the gentle dip of the regional discontinuity supports the hypotheses that the deposition rate of the RTS may have been slightly greater near the center of PL and/or that the erosional rate of the same sequence was slightly greater near the margins of PL.

At the same time, angular unconformities seem to be present also in the buried portion of the SPLD in PL (cf. Figs. 5-9). This suggests that a large area around the PL and beyond the marginal scarps of the region has undergone erosion or non-deposition. The radar unconformities have an elevation range (about 1900-2000 m) consistent with the elevation of the similar structures exposed on the PL margins. Thus, we infer that also the buried angular unconformities are consistent with the AUR1.

Based on the analysis of *Kolb and Tanaka* [2006], the AUR1 should be older than a higher regional discontinuity located at the base of a third most recent SPLD sequence (i.e., Aa2 unit). This discontinuity can be inferred in some peripheral outcrops of PL [*Kolb and Tanaka,* 2006], close to the poleward borders of Promethei Chasma and Chasma Australe (in L2, L5, L17, L18, L20 logs; Fig. A11), where there is a local increase in the thickness of the SPLD (Fig. 1a, c). Nevertheless, this bounding surface, located at a presumed elevation >2300 m, has not clearly been observed in the analyzed region. One possible exception is in one marginal outcrop (e.g., L2; cf. Table 1) in which it cannot be distinguished with confidence due to limitations (in terms of quality/resolution and areal coverage) of the dataset. On the contrary, this structure has not been observed in radargrams because the rough topography of the likely region in which it is supposed to be would prevent SHARAD to see eventual reflectors. We appointed this uncertain discontinuity as AUR2.

The local observed unconformities at lower (~1400 m; AUL1; cf. Table 1 and Fig. A1) and higher (~2300 m; AUL2; cf. Table 1 and Fig. A1) elevations than the AUR1 are apparently unrelated to this latter and the AUR2 regional surfaces. These unconformities (for the most uncertain) seem to bound sequences of minor-order rank without lateral continuity at regional scale. Although they should imply a further complexity of the SPLD stratigraphy, given their uncertainty and absence of lateral continuity, they do not allow the definition of minor-order discontinuity-bounded sequences [e.g., *Chang*, 1975]. Thus, they were not considered in the definition of the regional stratigraphy of PL.

3.2. Definition of the "AUR1-bounded" units and regional stratigraphy of PL.

Based on the previous observations and assumptions we can define two formal regional "discontinuity-bounded" units or Synthems in the SPLD in PL (Fig. 15). These units are separated by the AUR1 discontinuity and are named, respectively:

1) Promethei Lingula 1 unit (PL1), coinciding with the RTS morphologic sequence;
2) Promethei Lingula 2 unit (PL2), coinciding with the SSS morphologic sequence.

Based on the available dataset and the good exposure of the layers, the stratigraphic sequence L7b (Figs. 1a, 10-12) is assumed to be representative of the regional PL stratigraphy and was thus chosen as a type section. This section best preserves the layered stack and acts as reference point for analyzing the regional stratigraphy and for comparing and correlating the exposed sections across the region. It is located in the northeastern margins of PL (latitude 79.31°S, longitude 102.23°E; cf. Figs. 1a and Table 1).

The regional stratigraphy of PL is obtained correlating across the PL region the L7b with the other sections through the defined AUR1 discontinuities. The lower, older PL1 unit (Fig. 15) is exposed only along the PL scarps. It is confined at its bottom by an inferable non-conformity surface with the Late Noachian and Hesperian bedrock [*Tanaka et al.* 2014] and at its top by the AUR1 discontinuity. The PL1 is characterized by a maximum thickness of ~800-1000 m and is located in the vicinity of Promethei Chasma (L20, Fig. 15) in the inland PL and along some sectors of the PL margins, primarily corresponding to the L7 section (Fig. 15). Following the AUR1 elevation trend, the PL1 thickness significantly decreases toward the margins of the ice sheet, where erosion was focused, to a minimum of 250 m measured in the L6 section. This unit is consistent with the Aa1a member of *Kolb and Tanaka* [2006], observed by them only in Promethei and Ultimum Chasmata.

The PL2 (Fig. 15) is confined at its bottom by the AUR1 discontinuity and at its top by the topographic surface or, possibly, by the AUR2 discontinuity. The PL2 is consistent with the locally observed Aa1b member of *Kolb and Tanaka* [2006]. The possible different attitudes of the bedding planes of the two units in both visible and radar images demonstrate that the PL2 was deposited atop the irregular upper surface of the PL1. The unit PL2 may reach a maximum thickness of ~900-1000 m (L17). Unlike for the PL1, the logs indicate that thicker sequences are primarily located near the PL margins (i.e., L5, L9, L10, L17, L18). Again, this may be because after the PL2 deposition and during the formation of Australi Sulci by wind ablation [*Kolb and Tanaka*, 2006], erosion was primarily focused on the central parts of the PL and removed part of the PL2 after its deposition. It is also possible that the PL2 deposition was not homogeneous over PL and was instead focused, for some unknown reason, on its margins. This last interpretation could be suggested by radargrams, in which more net accumulation (sum of net deposition and erosion) seems to have occurred on the sides of PL (e.g. ESE side in Fig. 9).

According to *Kolb and Tanaka* [2006], a further unit (Aa2) could unconformably overlie the PL2 in the Promethei and Ultimum Chasmata region (logs L17, L18, L20), near the Australi Sulci and on the poleward side of the Chasma Australe (log L5), separated by the AUR2. Thus, PL region has been only marginally interested by youngest depositional events. Alternatively, the absence of the Aa2 in the strict PL lobe suggests its complete removal by erosion or non-deposition. Moving from the PL inland (A-A' profile) toward the PL margins (B-B' profile) in Fig. 15, the average thickness of the SPLD sequence decreases from approximately 1700 m to approximately 1200 m. This can be explained through some combination of the following:

1) The ice-dome physiography, which is usually characterized by a depositional rate higher at its center (“accumulation-like zone”) than at its margins (“ablation-like zone”). This would explain

the slight dip angle at the regional scale of the SPLD toward the periphery of the ice dome, as stated by *Byrne and Ivanov* [2004] and suggested by the radargrams;

2) The presence, toward the central ice dome, of the overlying unit Aa2, according to mapping done by *Kolb and Tanaka* [2006];

3) The heterogeneous erosion of the SPLD unit, primarily focused along the PL margins. This trend is reversed in the Australe Sulci region (EW profile), where the average thickness of the SPLD sequence is lower than in the PL margins. This is consistent with a high rate of erosion in the region due to katabatic winds, as suggested by *Koutnik et al.* [2005] and *Kolb and Tanaka* [2006].

3.3. Some possible climatic implications

As introduced in Section 1, unconformities are important markers of the growth and retreat of the Polar Layered Deposits in both hemispheres. They indicate that global or regional climate changes affected Mars at various times in its recent history [*Fishbaugh et al.*, 2008], likely induced by variations in Mars orbital parameters, in particular its spin axis obliquity [*Levrard et al.*, 2007; *Greve et al.*, 2010; *Forget et al.*, in press, 2017]. Mars's obliquity indeed varies by about ±10° with a 10^5 year cycle, around a mean value (currently 25°) which is thought to have changed by several tens of degree in the past [*Laskar and Robutel*, 1993; *Touma and Wisdom*, 1993; *Laskar et al.*, 2004]. The resulting climate changes were studied by *Toon et al.* [1980] and *Jakosky and Carr* [1985] on the basis of energy balance calculations, and explored in more details by numerical global climate models able to simulate Mars water cycle [*Mischna et al.*, 2003; *Levrard et al.*, 2004; *Montmessin et al.*, 2005; *Forget et al.*, 2006; *Levrard et al.*, 2007; *Madeleine et al.*, 2014]. These studies demonstrated that, while surface water ice is only stable in the polar regions on present-day Mars, large amount of water ice could have accumulated at lower latitudes at the expense of the polar reservoirs when the obliquity was higher, forming all sorts of glaciers-related landforms and ice mantles, which remnants can still be observed today. To first order, the ice-rich strata of the Polar Layered Deposits result from the accumulation of ice in the polar regions when the climate conditions (low mean obliquity) favored ice accumulation in the polar regions, while unconformities corresponds to periods of net ice sublimation at the poles, resulting in the formation of irregular erosion.

In the Northern hemisphere, several studies have linked the stratigraphy observed in surface images [e.g. *Laskar et al.*, 2002; *Levrard et al.*, 2007; *Hvidberg et al.*, 2012] and radargrams [e.g. *Putzig et al.*, 2009] with the variations of Mars' obliquity and orbital parameters calculated for the past 5 million year. Before ~5 Ma, the mean obliquity was higher than today and its values oscillated between 25° and 45° [e.g. *Laskar et al.*, 2002; 2004]. In such conditions, climate models predict that the ice-rich NPLD could not persist stably at the surface and that they slowly accumulated after 4 million years ago [*Levrard et al.*, 2007; *Greve et al.*, 2010] when the mean obliquity decreased. While the details of the stratigraphy are not yet fully understood, *Levrard et al.* [2007]'s model was recently found to successfully predict the upper 300 m of the NPLD cap (and the major discontinuity below), thought to have accumulated since ~370,000 years ago [*Smith et al.*, 2016].

Compared to the NPLD, the Southern Polar Layered Deposits are more difficult to understand for two reasons:

1) According to the cratering record, the age of the SPLD surface ranges between ~30 to 100 Myr [*Plaut et. al.*, 1988; *Herkenhoff and Plaut*, 2000; *Koutnik et al.*, 2002]. Thus, they accumulated during periods for which no orbital and obliquity data are available, because of the inherent chaotic nature of the evolution of the Martian obliquity [e.g., *Laskar et al.*, 2004]. Chaos prevent the extrapolation of the Martian spin/orbit history before ~10-20 My ago [*Laskar and Robute*, 1993; *Touma and Wisdom*, 1993]. Thus, we can only speculate about the variations of the mean obliquity at the time of the formation of the SPLD, guided by the statistical studies performed by *Laskar et al.* [2004]. In fact, studying the stratigraphy of the SPLD might ultimately enable us to observationally constrain the obliquity history.

2) According to models, the Mars climate system tends to favor the accumulation of water ice in

the Northern Polar Regions rather than in the South, because of the topographic asymmetry between the Southern and Northern hemisphere. The global north-south elevation difference favors a dominant southern summer Hadley circulation (responsible for the inter-hemispheric transport of water) [*Richardson and Wilson*, 2002b] and may also prevent the formation of a Northern "dusty season" and the related atmospheric warming when the perihelion was opposite of today (i.e. during Northern winter; *Montmessin et al.* [2005]). Admittedly, *Montmessin et al.* [2005] showed that every 50 000 years there are periods when Mars eccentricity permit the accumulation of ice in the Southern Polar regions at the expense of the NPLD. This is when Mars perihelion occurs during Northern summer (the opposite of today's conditions), resulting in a more intense sublimation of the NPLD due to increased insolation. However, the amount of ice then accumulated in the southern polar region should only reach a few meters at most [*Montmessin et al.*, 2005]. On average, the present-day Mars climate system seems to only allow the formation of thick Polar Layered deposits in the North. This explains why the NPLD are much more recent than the SPLD, but raises a question: in which conditions did ice accumulate at the South Pole to form the 3 km-thick SPLD?

A first possibility could be that, when the SPLD formed, the atmospheric pressure was significantly higher than today. With a thick enough atmosphere, atmospheric adiabatic cooling can influence the surface and near-surface temperature and favor ice accumulation in the high altitude south polar region rather the northern plain, just like on Earth today. This process was invoked to explain the origin of the Dorsa Argentea Formation, a Hesperian southern polar ice cap now buried by sediments [*Wordsworth et al.*, 2013]. On present-day Mars, the atmosphere is too thin to affect the surface temperature and the local topography has no significant effect on surface temperature *Forget et al.* [2013]. The transition between a ‘‘present-day Mars regime’’ and an ‘‘Earth-like regime’’ was investigated by *Forget et al.* [2013], who showed that at least 100 mbar is needed to affect surface temperatures and thus ice stability. This is probably unlikely for Mars in the past 200 Millions years [*Forget et al.*, 2017 in press].

A more likely possibility is that the Southern Polar Layered Deposits formed during periods when the water cycle was so important that ice accumulated in both the northern and southern polar regions. For instance, this could have occurred when large amounts of tropical or mid-latitude water ice were available to sublime and the obliquity low enough to favor net condensation of water ice at the poles [*Levrard et al.,* 2004; *Madeleine et al.*, 2009]. From that point of view it is interesting to note that the largest non-polar glacier related landforms observed on Mars do not date from the past 10 millions of year, but rather seems to have evolved to their present-day aspect 30 to 100 millions years ago, the approximate age of the SPLD [e.g., *Herkenhoff and Plaut*, 2000; *Koutnik et al.* 2002]. This includes the Mid-Latitude Lobate Debris Aprons and Lineated Valley Fills, the Mid-High Latitude Concentric Crater Fill, or the Tropical Mountain Glaciers (see *Head and Marchant* [2009]; *Forget et al.* [2017], and reference therein). Another key type of landforms are the mid-latitudes "pedestal craters" which are impact craters perched on a decameters thick pedestal interpreted to be the remnant of ice-rich deposit locally armored from erosion by the cratering event. The presence of thousands of pedestal craters poleward of 30° latitude suggest the presence of very extensive, decameters thick, water ice deposits covering the mid to high latitudes in the past [*Kadish and Head*, 2010]. *Kadish and Head* [2014] calculated a wide range of crater size-frequency distribution ages for the formation of the pedestal crater but showed that 70% of the pedestal ages are less than 250 Myr old. During the 150 Myr period between 25 Ma and 175 Ma, they found at least one pedestal age every 15Ma.

Likely, the SPLD formed on a very ice-rich planet Mars possibly covered by decameters thick ice deposits overall the mid-latitudes and extensive glaciers in the tropics. They recorded climatic events from a very different period than the ones archived in the NPLD, although it is not possible to exclude at all that climate during the formation of the SPLD (about 100 Ma) was similar to climate 5-0 Ma. In any case, another point of evidence for a very different evolution of the SPLD compare to the NPLD is the presence of massive deposits of CO_2 ice in the Planum Australe, but not in the Planum Boreum [*Phillips et al.*, 2011].

While it is premature to attribute an absolute age to the recorded events and to quantitatively constrain the obliquity history of Mars, analyzing the stratigraphy of Promethei Lingula allows to investigate major depositional and erosional events. Moreover, the SPLD are likely much older than the NPLD and they may represent a unique record not found elsewhere. Thus, as introduced, their stratigraphy contributes to a more refined understanding of climate change during the Late Amazonian on Mars. For instance, we can note that the discontinuity AUR1 represents a clear change in the environmental conditions of PL, interrupting the local continuity in the SPLD deposition. AUR1 can be related to a primary erosional or non-depositional event (by sublimation, melting, wind abrasion, and/or the absence or reduction of solid precipitation/condensation) taking place between two main depositional stages by solid precipitation/condensation and wind accumulation of the SPLD. Fig. 16 illustrates the overall evolution of the PL region and the different climatic phases, as described below:

Time 0 (Fig. 16a). During a first climatic period, the unit PL1 was deposited and the PL ice-sheet reached its maximum advance, probably as a result of the instability of large tropical and mid-latitude ice reservoir at relatively low obliquity.

Time 1 (Fig. 16b). During another insolation period (from lower to higher obliquity (E1), a climatic change began that warmed the polar regions on average. This would have determined an extensive erosional stage of the PL1 sequence, forming the AUR1. For simplicity, assuming that the gentle regional dip angle of the AUR1 (0.05°-0.1°) is only due to the inhomogeneous erosion rate removing the PL1 (and thus also assuming a homogeneous thickness of the PL1 before the AUR1 formation), it is possible to estimate that the possible maximum thickness of material removed across the length of PL (approximately 350-400 km) was ~300-600m. The warm temperatures at this time [*Constard et al.,* 2002] may have induced local melting and broad deformation of the SPLD (wet conditions), which in turn affected the attitude of the layers and possibly triggered or accelerated an inhomogeneous outward movement of the PL ice sheet [e.g. *Guallini et al.*, 2012; 2014].

Time 2 (Fig. 16c). From high to low average obliquity. A new, gradual decrease of the rotational axis to lower angles (D2) brings about a new drop in mean surface temperature at polar latitudes and, assuming that ice is still available at lower latitudes, the beginning of the deposition of the unit PL2 upon the PL1. The accumulation of the PL2 followed the existing topography of the AUR1, resting upon it both with conformable and unconformable contacts.

Time 3 (Fig. 16d). From low to high average obliquity. This episode was followed by a period of erosion of the PL2 (from low to high obliquity; E2), which was likely combined with a reduction in or absence of precipitation, causing a negative mass balance of the PL ice sheet. Particularly at the inland PL, close to the high surface topography of the ice dome, katabatic winds removed material from the SPLD [*Koutnik et al.*; 2005], forming the Australe Sulci [*Kolb and Tanaka*; 2006] and removing significant volumes of the PL2. Based on evaluations of the Australe Sulci region done by *Kolb and Tanaka* [2006] and the stratigraphic correlation of outcrops along NS and EW profiles (cf. Fig. 15), up to 300-500 m of the PL2 was possibly removed.

Time 4 (Fig. 16e). From high to low average obliquity. During the transition from high obliquity to the present-day low obliquity, a new depositional stage formed the Aa2 unit [*Kolb and Tanaka*; 2006], perhaps mostly outside of PL and divided from the PL2 by the inferred regional unconformity AUR2. The deposition of the unit occurred at latitudes higher (i.e., ~80° latitude) than the PL region, which may only have been marginally buried by the Aa2, and was quickly followed by renewed widespread erosion of the SPLD (E3). According to *Koutnik et al.* [2005] and *Milkovich and Plaut* [2008], this latter erosional phase, which is primarily characterized by dry conditions and dust accumulation, occurred in a climate similar to that of the present day (i.e., warmer temperatures are not required). As suggested by the medium-high dip angles of the SPLD scarps [*Milkovich and Plaut*; 2008], erosional processes are still ongoing by wind ablation and sublimation. According to *Byrne* [2009] and given the uncertainties, we assume that the preservation of the SPLD through periods of high obliquity could be explained if the sublimation and melting of water ice is a self-limiting process. In particular, surface dust lag caused by the removal of the volatile water ice may retard sublimation of the underlying ice when the dust is thick enough.

As previously described, the complexity of the stratigraphy suggests that minor-order periods of erosion and deposition also characterized the evolution/growth of the SPLD, possibly driven by other factors, however barely definable using the available dataset. These minor-order episodes resulted in the development of local angular unconformities, to which the AUL1 and AUL2 likely belong, affecting some sections of the PL. As instance, we can suppose that topography might have locally influenced the deposition and erosion of the SPLD [e.g. *Smith et al.*, 2013] secondary to the PL1, PL2 and AUR1-AUR2(?) formation. In fact, when SPLD dome accumulated, topographic relief increased, increasing the likelihood of katabatic wind flow, driven by gravity. These latter are capable to erode material from the slopes and redeposit it elsewhere. Nevertheless, eventual minor-order factors of erosion and deposition of PL might suggest that, from place to place, the quantity of growth/retreat of the SPLD changed in function of local scale factors, however lying within the same regional context, driven by global factors.

4. Conclusions

We performed a stratigraphic analysis of the SPLD in Promethei Lingula based on the identification of unconformities, the use of correlative discontinuities and conformities and the morphologic description of the sequences both in visible images and radargrams. Using techniques commonly used in Earth-based studies, this approach constrains the stratigraphy of the region and tries to reduce the amount of possible ambiguous interpretations that are exclusively based on “morpho-stratigraphy”. In this regard, our approach is an attempt to bypass the problems related to the morphologic and radiometric appearance of the layers. Thus, it does not exclude diverse classifications but complements them, whereas other stratigraphic analyses are doubtful, awkward or impossible to define.

We identify two main depositional events that formed two stratigraphic units, named PL1 and PL2; these are interrupted by one main erosional or non-depositional phase marked by the discontinuity AUR1. Subsequently, less extensive events partially eroded the PL2, possibly forming the AUR2 discontinuity, and then formed the Aa2 unit [*Kolb and Tanaka*, 2006], which is almost entirely located outside the PL ice sheet. Both radar datasets and visible images are consistent with this interpretation, which supports and extends to the entire PL region the stratigraphy proposed by *Kolb and Tanaka* [2006] for the areas of Australi Sulci and Promethei and Ultimum Chasmata. Thus, the PL1 and PL2 sequences have the rank of major-order units (i.e., Synthems) because the AUR1 makes them mappable at regional scale. Secondary members within major-order units cannot be defined through allostratigraphic criteria.

In optical images, the lower PL1 is characterized by a prevalent "ridge and trough" (RTS) [*Malin and Edgett*, 2001] morphology, given by a succession of thin layers having diverse erosional strengths and brightness. The upper PL2 is characterized primarily by a "stair-stepped" morphology (SSS) [*Malin and Edgett*, 2001] and is outlined by thicker layers than in the PL1, with no evident variations in brightness or erosional textures. However, at the regional scale, the PL2 has a slight lateral variability in morphology, showing minor-order "ridge and trough" sequences in some locations (e.g., Chasma Australe).

The AUR1 is also inferable in several radargrams at SHARAD wavelengths. Both PL1 and PL2 sequences show bright reflectors and horizontal non-reflective zones.

The PL stratigraphy supports the hypothesis of time-varying climatic conditions at polar latitudes that controlled the SPLD geologic history. These climatic conditions are marked by alternating depositional and erosional/not depositional stages and possibly also by changes in the depositional pattern and erosional style of the PL1 and PL2 units. The quasi-cyclical variation of some orbital parameters (such as the variation of the obliquity of the Martian rotational axis) may have determined climate changes. In particular, the AUR1 formed during high angle orbital axis [e.g., *Costard et al*. [2002], causing a high insolation of the SPLD surface. In this regard: 1) The main-order stratigraphy of each PL unit (PL1 and PL2) originated under one long-period insolation period, forced by one broad variation in Martian obliquity. From high to low obliquity, the erosion progressed to deposition. From low to high obliquity, deposition progressed to erosion. It is possible that this long-period insolation period was affected by a positive feedback interaction with other shorter-period orbital variations. 2) During the occurrence of the first episode, the AUR1 erosional surface formed under increasing obliquity [*Jarosky et al.*, 1995; *Milkovich and Head*, 2005] and causing regional-scale erosion of the PL1. 3) During the main-order insolation periods, minor-order orbital variations affected the deposition of the PL1 and PL2, resulting in multiple sub-sequences [e.g., *Milkovich and Head*, 2005] and possibly local-scale unconformities (e.g., the AUL1/AUL2) or depositional lags. 4) A third insolation half-cycle (from high to low obliquity) deposited the Aa2 unit and brought the planet to present-day conditions (low-obliquity period).

In conclusion, the present study proposes a simple model of SPLD formation at the PL regional scale due to alternating depositional and erosional stages and driven by climate changes due to orbital variation. In this way, main-order sequences, in turn related to geologic controlling factors, are defined. Given the complexity of the SPLD stratigraphy, several minor-order distinct periods of accumulation and erosion can be (and have been) defined using different approaches, also in other regions of the southern ice dome [e.g., *Milkovich and Plaut*, 2008; *Limaye et al.*, 2012], completing the overall description of the SPLD stratigraphy in the Planum Australe.

Acknowledgments

Our research was funded by the Italian Space Agency (ASI) and the Italian Ministry of University and Research (MIUR). This manuscript was completed and implemented thanks to the National Centers of Competence in Research (NCCRs) PlanetS grant. The authors wish to thank the International Space Science Institute (ISSI, Bern, Switzerland) for the kind hospitality during the preparation of part of this manuscript. We are in debt also to Dr. Monica Pondrelli and Prof. Gian Gabriele Ori (IRSPS, Università d'Annunzio, Pescara, Italy), and to Dr. Simone Silvestro (SETI Institute, CA, USA) for the constructive discussions and advices. Special thanks to the Italian SHARAD team for the acquired data and for the support to our work. We also greatly thank two anonymous reviewers for their constructive comments and suggestions that substantially improved

the manuscript.

References

Anguita, F., B. Rosa, B. Gerardo, D. Gomez, A. Collado, and J.W. Ricef (2000), Chasma Australe, Mars: structural frame work for a catastrophic outflow origin. *Icarus*, 144, 302-312, doi: 10.1006/icar.1999.6294.

Bates, R.L., and J.A. Jackson (1987). Glossary of Geology, P. 788, 3rd Ed. American Geological Institute, Alexandria, Virginia.

Burrough, P. A. (1986), *Principles of Geographical Information Systems for Land Resources Assessment*. New York: Oxford University Press.

Byrne, S. (2009), The Polar Deposits of Mars, *Annu. Rev. Earth Planet. Sci.*, 37, 535-560, doi: 10.1146/annurev.earth.031208.100101.

Byrne, S., and A.B. Ivanov (2004), Internal structure of the Martian south polar layered deposits, *J. Geophys. Res.*, 109, 11001, doi: 10.1029/2004JE002267.

Byrne, S., K. Herkenhoff, P. Russell, C. Hansen, A. McEwen, and the HiRISE team (2007), Preliminary HiRISE polar geology results, abstract presented at *38th Lunar and Planetary Science Conference*, Houston, Texas, 1930.

Catuneanu, O. (2006), Principles of Sequence Stratigraphy, p. 376, Elsevier, Amsterdam, The Netherlands.

Chang, K.H. (1975), Unconformity-bounded stratigraphic units, *Geol. Soc. of Amer. Bull.*, 86, 1544-1552, doi: 10.1130/0016-7606(1975)86<1544:USU>2.0.CO;2.

Christensen, P.R., B.M. Jakosky, H.H. Kieffer, M.C. Malin, H.Y. Mcsween Jr, K. Nealson, G.L. Mehall, S.H. Silverman, S.Ferry, M. Caplinger, and M. Ravine (2004), The Thermal Emission Imaging System (THEMIS) for the Mars 2001 Odyssey Mission, *Space Science Revie*ws, 110, 85–130, doi: 10.1007/978-0-306-48600-5_3.

Christian, S., J.W. Holt, S. Byrne and K.E. Fishbaugh (2013), Integrating Radar Stratigraphy with High Resolution Visible Stratigraphy of the North Polar Layered Deposits, Mars, *Icarus*, doi: 10.1016/j.icarus.2013.07.003.

Clifford, S.M., D. Crisp, D.A. Fisher, K.E. Herkenhoff, S.E. Smrekar, P.C. Thomas, D.D. Wynn-Williams, R.W. Zurek, J.R. Barnes, B.G. Bills, E.W. Blake, W.M. Calvin, J.M. Cameron, M.H. Carr, P.R. Christensen, B.C. Clark, G.D. Clow, J.A. Cutts, D.Dahl-Jensen, W.B. Durham, F.P. Fanale, J.D. Farmer, F.Forget, K.Gotto-Azuma, R. Grard, R.M. Haberle, W.Harrison, R. Harvey, A.D. Howard, A.P. Ingersoll, P.B. James, J.S. Kargel, H.H. Kieffer, J. Larsen, K. Lepper, M.C. Malina, D.J. McCleese, B. Murray, J.F. Nyea, D.A. Paigea, S.R. Platta, J.J. Plaut, N. Reeha, J.W. Rice Jr., D.E. Smith, C.R. Stoker, K.L. Tanaka, E. Mosley-Thompsona, T. Thorsteinssona, S.E. Wooda, A. Zent, M.T. Zuber, H. J. Zwally (2000), The state and future of Mars polar science and exploration, *Icarus*, 144, 210-242, doi: 10.1006/icar.1999.6290.

Costard, F., F. Forget, N. Mangold, and J.P. Peulvast (2002), Formation of recent martian debris flows by melting of near-surface ground ice at high obliquity, *Science*, 295, 110-113, doi: 10.1126/science.1066698.

Christian, S., Holt, J. W., Byrne, S. and Fishbaugh, K. E. (2013), Integrating radar stratigraphy with high resolution visible stratigraphy of the north polar layered deposits, Mars, *Icarus*, 226, 1241-1251, doi: 10.1016/j. Icarus.2013.07.003.

Cutts, J.A. (1973), Nature and origin of layered deposits in the martian polar regions, *J. Geophys. Res.*, 78, 4231-4249, doi: 10.1029/JB078i020p04231.

Cutts, J., and B. Lewis (1982), Models of climate cycles recorded in martian polar layered deposits, *Icarus*, 50, 216-244, doi: 10.1016/0019-1035(82)90124-5.

Dowedeswell, J., and S. Evans (2004), Investigations of the form and flow of ice-sheets and glaciers using radio-echo sounding, *Rep. Prog. Phys.*, 67, 1821-1861, doi:10.1088/0034-4885/67/10/R03.

Eisen, O., U. Nixdorf, and D. Wagenbach (2003), Alpine ice cores and ground penetrating radar: Combined investigations for glaciological and climatic interpretations of a cold Alpine ice body, *Tellus Ser. B.*, 55, 1007-1017, doi: 190.1034/j.1600-0889.2003.00080.x.

Fishbaugh, K., and C. Hvidberg (2006), Martian north polar layered deposits stratigraphy: Implications for accumulation rates and flow, *J. Geophys. Res.*, 111. doi: 10.1029/2005JE002571. E06012.

Fishbaugh, K.E., C.S. Hvidberg, D. Beaty, S. Clifford, D. Fisher, A. Haldemann, J.W. Head, M. Hecht, M. Koutnik, K. Tanaka, and W.J. Ammann (2008), Introduction to the 4th Mars polar science and exploration conference special issue: Five top questions in Mars polar science, *Icarus*, 196, 305-317, doi: 10.1016/j.icarus.2008.05.001.

Fishbaugh, K.E., S. Byrne, K.E. Herkenhoff, R.L. Kirk, C. Fortezzo, P.S. Russell, and A. McEwen (2010), Evaluating the meaning of "layer" in the martian north polar layered deposits and the impact on the climate connection, *Icarus*, 205, 269-282, doi: 10.1016/j.icarus.2009.04.011.

Forget, F., R.M. Haberle, F. Montmessin, B. Levrard, and J.W. Head (2006), Formation of glaciers on Mars by atmospheric precipitation at high obliquity, *Science*, 311, 368–71, doi: 10.1126/science.1120335.

Forget, F. S. Byrne, J. W. Head, M. A. Mischna, N. Schörghofer (2017, in press), Recent Climate Variations, in *The Atmosphere and Climate of Mars*, Cambridge University Press.

Greve, R., Grieger, B. and Stenzel, O. J. (2010), MAIC-2, a latitudinal model for the Martian surface temperature, atmospheric water transport and surface glaciation, Planetary and Space Science, 58, 931-940, doi: 10.1016/j.pss.2010.03.002.

Grima, C., F. Costard, W. Kofman, B. Saint-Bézar, A. Servain, F. Rémy, J. Mouginot, A. Herique, and R. Seu (2011), Large asymmetric polar scarps on Planum Australe, Mars: characterization and evolution, *Icarus*, 212(1), 96-109, doi: 10.1016/j.icarus.2010.12.017.

Guallini, L., A.P. Rossi, L. Marinangeli (2010), "Unconformity-bounded" Units on Mars SPLD (Promethei Lingula): a first step towards formal stratigraphic classification?, abstract presented at *41st Lunar and Planetary Science Conference*, Houston, Texas, 1721.

Guallini, L. (2012), New geologic constraints on South Polar Layered Deposits (Promethei

Lingula region) and Light-Toned Layered Deposits (Iani Chaos region): Two different facets of an ancient water activity and climate dynamic on planet Mars, Ph.D. thesis, IRSPS, Dip. di Scienze, Univ. d'Annunzio, Pescara, Italy.

Guallini, L., F. Brozzetti, and L. Marinangeli (2012), Large-scale Deformational Systems in the South Polar Layered Deposits (Promethei Lingula, Mars): "Soft-Sediment" and Deep-Seated Gravitational Slope Deformations Mechanisms, *Icarus*, 220, 821-843, doi:10.1016/j.icarus.2012.06.023.

Guallini, L., Pauselli, C., Brozzetti, F. and Marinangeli, L. (2014), Physical Modeling of Large-scale Deformational Systems in the South Polar Layered Deposits (Promethei Lingula, Mars): New Geologic Constraints and Climatic Implications. From Platz, T., Massironi, M., Byrne, P. K. & Hiesinger, H. (eds), *Volcanism and Tectonism Across the Inner Solar System*. Geological Society, London, Special Publications, 401, http://dx.doi.org/10.1144/SP401.13.

Gwinner, K., F. Scholten, F. Preusker, S. Elgner, T. Roatsch, M. Spiegel, R. Schmidt, J. Oberst, R. Jaumann, and C. Heipke (2010), Topography of Mars from global mapping by HRSC high-resolution digital terrain models and orthoimages: Characteristics and performance, *Earth Planet. Sci. Lett.*, 294, 506-519, doi:10.1016/j.epsl.2009.11.007.

Haberle, R.M., J.R. Murphy, and J. Schaeffer (2003), Orbital change experiments with a Mars general circulation model, *Icarus*, 161, 66– 89, doi: 10.1016/S0019-1035(02)00017-9.

Haberle, R.M., F. Montmessin, M.A. Kahre, J.L. Hollingsworth, et al. (2011), Radiative effects of water ice clouds on the Martian seasonal cycle. In: Fourth International Workshop on the Mars Atmosphere: Modelling and Observations Abstracts, pages 223-225.

Head, J.W., J.F Mustard, M.A. Kreslavsky, R.E. Milliken, and D.R. Marchant (2003), Recent ice ages on Mars, *Nature*, 426, 797-802, doi: doi:10.1038/nature02114.

Heggy, E., S.M. Clifford, A. Younsi, J. L. Miane, R. Carley, and R. V. R. Morris (2007), On the Dielectric Properties of Dust and Ice-Dust Mixtures: Experimental Characterization of the Martian Polar-layered Deposits Analog Materials, abstract presented at *38th Lunar and*

Planetary Science Conference, Houston, Texas, 1756.

Herkenhoff, K., and B. Murray (1990), High-resolution topography and albedo of the south polar layered deposits on Mars, *J. Geophys. Res.*, 95, 14511-14529, doi: 10.1029/JB095iB09p14511.

Herkenhoff, K.E., and J.J. Plaut (2000), Surface ages and resurfacing rates of the polar layered deposits on Mars, *Icarus*, 144, 243-255, doi: 10.1006/icar.1999.6287.

Herkenhoff, K.E., S. Byrne, P.S. Russell, K.E. Fishbaugh, and A.S. McEwen (2007), Meter-scale morphology of the north polar region of Mars, *Science*, 317, 1711, doi: 10.1126/science.1143544.

Hvidberg, C.S., K.E. Fishbaugh, M. Winstrup, A. Svensson, S. Byrne, and H.E. Herkenhoff (2012), Reading the Climate Record of the Martian Polar Layered Deposits, *Icarus*, 221, 406-419, doi: 10.1016/j.icarus.2012.08.009.

Kargel, J.S., and K.L. Tanaka (2002), The martian south polar cap: glacial ice-sheet of multiple interbedded ices, abstract presented at *33rd Lunar and Planetary Science Conference*, Houston, Texas, 1799.

Kieffer, H.H., S.C. Chase, T.Z. Martin, E.D. Miner, and F.D. Palluconi (1976), Martian north pole summer temperatures: Dirty water ice, *Science*, 194, 1341-1344, doi: 10.1126/science.194.4271.1341.

Kolb, E.J., and K.L. Tanaka (2000), Possible melt-water lakes beneath Planum Australe, Mars: predictions based on present and past polar deposits, abstract presented at *First International Conference on Mars Polar Science and Exploration*, Houston, Texas, 4107, 95.

Kolb, E.J., and K.L. Tanaka (2001), Geologic history of the polar regions of Mars based on Mars global surveyor data. II. Amazonian period, *Icarus*, 154, 22-39, doi: 10.1006/icar.2001.6676.

Kolb, E.J., K.L. Tanaka (2006), Accumulation and erosion of south polar layered deposits in the Promethei Lingula region, Planum Australe, Mars, *MARS*, 2, 1-9, doi: 10.1555/mars.2006.0001.

Koutnik, M., S. Byrne, and S. Murray (2002), South polar layered deposits of Mars: The cratering record, *J. Geophys. Res.*, 107, 1029, doi: 10.1029/2001JE001805.

Koutnik, M.R., S. Byrne, B.C. Murray, A.D. Toigo, and Z.A. Crawford (2005), Aeolian controlled modification of the Martian south polar layered deposits, *Icarus*, 174, 490-501, doi: 10.1016/j.icarus.2004.09.015.

Jakosky, B. M., Henderson, B. G., and Mellon,T., M. (1993), The Mars water cycle at other epochs: recent history of the polar caps and layered terrain, *Icarus*, 102, 286-297.

Jakosky, B.M., B.G. Henderson, and M.T. Mellon (1995), Chaotic obliquity and the nature of the Martian climate, *J. Geophys. Res.*, 100(E1), 1579-1584, doi: 10.1029/94JE02801.

Lalich, D. E. and Holt, J. W. (2016), New Martian climate constraints from radar reflectivity within the north polar layered deposits, Geophys. Res. Lett., 2016GL071323, doi: 10.1002/2016GL071323.

Laskar, J. and Robutel, P. (1993), The chaotic obliquity of the planets, *Nature*, 361, 608-612.

Laskar, J., B. Levrard, and J.F. Mustard (2002), Orbital forcing of the martian polar layered deposits, *Nature*, 419, 375-377, doi: 10.1038/nature01066.

Laskar, J., A.C.M. Correia, M. Gastineau, F. Joutel, B. Levrard, and P. Robutel (2004), Long term evolution and chaotic diffusion of the insolation quantities on Mars, *Icarus*, 170, 343-364.

Levrard, B., F. Forget, F. Montmessin, and L. Laskar (2004), Recent ice-rich deposits formed at high latitudes on Mars by sublimation of unstable equatorial ice during low obliquity, *Nature*, 431, 1072–1075, doi: 10.1038/nature03055.

Levrard, B., F. Forget, F. Montmessin, and L. Laskar (2007), Recent formation and evolution of northern Martian polar layered deposits as inferred from a global climate model, *J. Geophys. Res.*, 112:6012, doi: 10.1029/2006JE002772.

Li, J., Andrews-Hanna, J. C., Sun, Y., Phillips, R. J., Plaut, J. J. and Zuber, M. T. (2012), Density variations within the south polar layered deposits of Mars, J. Geophys. Res., 117, E04006, doi: 10.029/2011JE003937.

Limaye, A.B.S., O. Aharonson, and J. T. Perron (2012), Detailed stratigraphy and bed thickness of the Mars north and south polar layered deposits, *J. Geophys. Res.*, 117, E06009, doi:10.1029/2011JE003961.

Madeleine, J-B. F. Forget, J. W. Head, B. Levrard, F. Montmessin, and E. Millour (2009), Amazonian northern mid-latitude glaciation on Mars: A proposed climate scenario, *Icarus*, 203:390-405.

Madeleine, J.-B., J. W. Head, F. Forget, et al. (2014), Recent ice ages on Mars: The role of radiatively active clouds and cloud microphysics, *Geophys. Res. Lett.*, 41, 4873–4879.

Malin, M., and K. Edgett (2001), Mars Global Surveyor Mars Orbiter Camera: Interplanetary cruise through primary mission, *J. Geophys. Res.*, 106 (E10), 23429-23570, doi: 10.1029/2000JE001455.

Malin, M.C., J.F. Bell III, B.A. Cantor, M.A. Caplinger, W.M. Calvin, R.T. Clancy, K.S. Edgett, L. Edwards, R.M. Haberle, P.B. James, S.W. Lee, M.A. Ravine, P.C. Thomas, and M.J. Wolff (2007), Context Camera Investigation on board the Mars Reconnaissance Orbiter, *J. Geophys. Res.*, 112(EO5S04), doi: 10.1029/2006JE002808.

McEwen, A.S., E.M. Eliason, J.W. Bergstrom, N.T. Bridges, C.J. Hansen, W.A. Delamere, J.A. Grant, V.C. Gulick, K.E. Herkenhoff, L. Keszthelyi, R.L. Kirk, M.T. Mellon, S.W. Squyres, N. Thomas, and C.M. Weitz (2007), Mars Reconnaissance Orbiter's High Resolution Imaging Science Experiment (HiRISE), *J. Geophys. Res.*, 112(EO5S02), doi: 10.1029/2005JE002605.

Meentemeyer, R.K., and A. Moody, A. (2000). Automated mapping of conformity between topographic and geological surfaces. *Computers & Geosciences*, 26, 815-829, doi: 10.1016/S0098-3004(00)00011-X.

Mellon, M.T. (1996), Limits on the CO2 content of the martian polar deposits, *Icarus*, 124, 268-279, doi: 10.1006/icar.1996.0203.

Milkovich, S.M., and. J.W. III Head (2005), North polar cap of Mars: Polar layered deposit characterization and identification of a fundamental climate signal, *J. Geophys. Res.*, 110, E01005, doi:10.1029/2004JE002349.

Milkovich, S.M., and J.J. Plaut (2008), Martian south polar layered deposit stratigraphy and implications for accumulation history, *J. Geophys. Res.*, 113, 6007, doi: 10.1029/2007JE002987.

Milkovich, S.M., J.J. Plaut, A. Safaeinili, G. Picardi, R. Seu, R., and R.J. Phillips (2009), Stratigraphy of Promethei Lingula, south polar layered deposits, Mars, in radar and imaging data sets, *J. Geophys. Res.*, 114, E03002, doi: 10.1029/2008JE003162.

Mischna, M.A., M.I. Richardson, R.J. Wilson, and D.J. McCleese (2003), On the orbital forcing of Martian water and CO_2 cycles: A general circulation model study with simplified volatile schemes, *J. Geophys. Res.*, 108(E6), 5062, doi:10.1029/2003JE002051.

Mitchum, R. M. Jr., P.R. Vail, and S. Thompson III (1977). Seismic stratigraphy and global changes of sea-level, part 2: the depositional sequence as a basic unit for stratigraphic analysis, in Seismic Stratigraphy–Applications to Hydrocarbon Exploration, edited C. E. Payton, pp. 53–62, American Association of Petroleum Geologists Memoir 26.

Montmessin, F., Haberle, R. M., Forget, F., Langevin, Y., Clancy, R. T., and Bibring, J.-P. (2007), On the origin of perennial water ice at the south pole of Mars: A precession-controlled mechanism? *Journal of Geophysical Research (Planets)*, 112(E11), 8.

Murray, B.C., W.R. Ward, and S.C. Yeung (1973), Periodic insolation variations on Mars, *Science*, 180, 638-640, doi: 10.1126/science.180.4086.638.

Neukum, G., R. Jaumann, and the HRSC Co-Investigator Team (2004), HRSC: the High Resolution Stereo Camera of Mars Express, *ESA Special Publications*, SP-1240.

Nunes, D.C., and R.J. Phillips (2006), Radar subsurface mapping of the polar layered deposits on Mars, *J. Geophys. Res.*, 111, E06L21, doi: 10.1029/2005JE002609.

Oliver, M. A. (1990), Kriging: A Method of Interpolation for Geographical Information Systems, *International Journal of Geographic Information Systems*, 4: 313–332. 1990.

Perron, J., and P. Huybers (2009). Is there an orbital signal in the polar layered deposits on Mars?, *Geology*, 37 (2), 155–158, doi: 10.1130/G25143A.1.

Phillips, R.J., M.T. Zuber, S.E. Smrekar, M.T. Mellon, J.W. Head, K.L. Tanaka, N.E. Putzig, S.M. Milkovich, B.A. Campbell, J.J. Plaut, A. Safaeinili, R. Seu, D. Biccari, L.M. Carter, G. Picardi, R. Orosei, P. S. Mohit, E. Heggy, R. W. Zurek, A. F. Egan, E. Giacomoni, F. Russo, M. Cutigni, E. Pettinelli, J.W. Holt, C.J. Leuschen, and L. Marinangeli (2008), Mars North Polar Deposits: Stratigraphy, age, and geodynamical response, *Science*, 320 (5880), 1182-1185. doi: 10.1126/science.1157546.

Phillips, R.J., B.J. Davis, K.L. Tanaka, S. Byrne, M.T. Mellon, N.E. Putzig, R.M. Haberle, M.A. Kahre, B.A. Campbell, L.M. Carter, I.B. Smith, J.W. Holt, S.E. Smrekar, D.C. Nunes, J.J. Plaut, A.F. Egan, T.N. Titus, and R. Seu (2011), Massive CO2 Ice Deposits Sequestered in the South Polar Layered Deposits of Mars, *Science*, 332, 838-841, doi: 10.1126/science.1203091.

Plaut, J., R. Kahn, E. Guinness, and R. Arvidson (1988), Accumulation of sedimentary debris in the south polar region of Mars and implications for climate history, *Icarus*, 76, 357-377, doi: 10.1016/0019-1035(88)90076-0.

Plaut, J.J., G.Picardi, A. Safaeinili, A.B. Ivanov, S.M. Milkovich, A. Cicchetti, W. Kofman, J. Mouginot, W.M. Farrell, R.J. Phillips, S.M. Clifford, A. Frigeri, R. Orosei, C. Federico, I.P. Williams, D.A. Gurnett, E. Nielsen, T. Hagfors, E. Heggy, E.R. Stofan, D. Plettemeier, T.R. Watters, C.J. Leuschen, and P. Edenhofer (2007), Subsurface radar sounding of the south polar layered deposits of Mars, *Science*, 316, 92-96, doi: 10.1126/science.1139672.

Posamentier, H. W., and P.R. Vail (1988). Eustatic controls on clastic deposition II–sequence and systems tract models, in Sea Level Changes–An Integrated Approach, edited C. K. Wilgus, B. S. Hastings, C. G. St.C. Kendall, H. W. Posamentier, C. A. Ross and J. C. Van Wagoner, pp. 125–154, SEPM Special Publication 42.

Putzig, N. E., Phillips, R. J., Campbell, B. A., Holt, J. W., Plaut, J. J., Carter, L. M., Egan, A. F., Bernardini, F., Safaeinili, A., and Seu R. (2009). Subsurface structure of Planum Boreum from Mars Reconnaissance Orbiter Shallow Radar soundings, *Icarus*, 204, 443-457, doi: 10.1016/j.icarus.2009.07.034.

Reeh, N., H. Oerter, A. Letreguilly, H. Miller, and H.W. Hubberten (1991), A new, detailed ice-age oxygen-18 record from the ice-sheet margin in central West Greenland., *Palaeog. Palaeocl. Palaeoec.*, 4 (4), 373-383, doi: 10.1016/S0031-0182(12)80036-8.

Richardson, M.I., and R.J. Wilson (2002), Investigation of the nature and stability of the Martian seasonal water cycle with a general circulation model*, J. Geophys. Res.*, 107, 5031, doi: 10.1029/2001JE001536.

Russo, F., Cutigni, M., R. Orosei, C. Taddei, R. Seu, D. Biccari, E. Giacomoni, O. Fuga, and E. Flamini (2008), An incoherent simulator for the SHARAD experiment, *2008 IEEE Radar Conference, RADAR 2008*, 1-4, doi: 10.1109/RADAR.2008.4720761.

Salvador, A., and the International Subcommission on Stratigraphic Classification (1987), Unconformity-bounded stratigraphic units, *Geol. Soc. Amer. Bull.*, 98, 232-237, doi: 10.1130/0016-7606(1987)98<232:USU>2.0.CO;2.

Seu, R., D. Biccari, R. Orosei, L.V. Lorenzoni, R.J. Phillips, L. Marinangeli, G. Picardi, A. Masdea, and E. Zampolini (2004), SHARAD: the MRO 2005 shallow radar*, Planet. Space Sci.*, 52, 157-166, doi: 10.1016/j.pss.2003.08.024.

Seu, R., et al. (2007), Accumulation and erosion of Mars' South Polar Layered Deposits, *Science*, 317, 1715-1717, doi: 10.1126/science.1144120.

Simpson, B. (1968), Geological Maps, p. 98, Pergamon Press.

Sloss, L.L., W.C. Krumbein, and E.C. Dapples (1949). Integrated facies analysis, in Sedimentary facies in geologic history, edited C. R. Longwell, pp. 91–124, Geological Society of America Memoir 39.

Smith, D.E., R.J. Phillips, G. Alberti, D. Biccari, F. Bonaventura, M. Bortone, D. Calabrese, B.A. Campbell, M. Cartacci, L.M. Carter, C.Catallo, A. Croce, R. Croci, M. Cutigni, A. Di Placido, S. Dinardo, C. Federico, E. Flamini, F. Fois, A. Frigeri, O. Fuga, E. Giacomoni, Y. Gim, M. Guelfi, J.W. Holt, W. Kofman, C.J. Leuschen, L. Marinangeli, P. Marras, A. Masdea, S. Mattei, R. Mecozzi, S.M. Milkovich, A. Morlupi, J. Mouginot, R. Orosei, C. Papa, T. Paternò, P. Persi del Marmo, E. Pettinelli, G. Pica, G. Picardi, J.J. Plaut, M. Provenziani, N.E. Putzig, F. Russo, A.

Safaeinili, G. Salzillo, M.R. Santovito, S.E. Smrekar, B. Tattarletti, and D. Vicari (2001), Mars Orbiter Laser Altimeter: experiment summary after the first year of global mapping of Mars, *J. Geophys. Res.*, 106, 23689-23722, doi: 10.1029/2000JE001364.

Smith, M. R., Bandfield, J. L., Cloutis, E. A., and Melissa, S. R. (2013), Hydrated silica on Mars: Combined analysis with near-infrared and thermal-infrared spectroscopy, Icarus, 223, 633-648, doi: 10.1016/j.icarus.2013.01.024.

Squyres, S.W. (1979), The evolution of dust deposits in the Martian north polar region, *Icarus*, 40, 244-261, doi: 10.1016/0019-1035(79)90070-8.

Tanaka, K. L., Robbins, S. J., Fortezzo, C. M., Skinner Jr., J. A., and Hare, T. M. (2014), The digital global geologic map of Mars: Chronostratigraphic ages, topographic and crater morphologic characteristics, and updated resurfacing history, *Planetary and Space Science*, Planetary Geology Field Symposium, Kitakyushu, Japan, 2011: Planetary Geology and Terrestrial Analogs, 95, 11-24, doi: 10.1016/j.pss.2013.03.006.

Tanaka, K.L., and E.J. Kolb (2001), Geologic history of the polar regions of Mars based on Mars Global Surveyor data. I. Noachian and Hesperian periods, *Icarus*, 154, 3-21, doi: 10.1006/icar.2001.6675.

Tanaka, K.L., and D.H. Scott (1987), *Geologic map of the polar regions of Mars*, in the Map I-1802-BC, U.S. Geol. Surv. Misc. Invest. Ser.

Thomas, P., S. Squyres, K. Herkenhoff, A. Howard, and B. Murray (1992), Polar deposits of Mars, in Mars, 23, edited by H.H. Kieffer et al., pp. 767-795, University of Arizona Press, Tucson.

Toon, O.B., J.B. Pollack, W. Ward, J.A. Burns, and K. Bilski (1980), The astronomical theory of climate change on Mars, *Icarus*, 44, 552-607, doi: 10.1016/0019-1035(80)90130-X.

Touma, J. and Wisdom, J. (1993) The chaotic obliquity of Mars, *Science*, 259, 1294-1297.

Van Wagoner, J. C. (1995), Overview of sequence stratigraphy of foreland basin deposits: terminology, summary of papers, and glossary of sequence stratigraphy, in Sequence Stratigraphy of Foreland Basin Deposits, edited J. C. Van Wagoner and G. T. Bertram, pp. ix-xxi, American

Association of Petroleum Geologists Memoir 64.

Ward, W.R. (1973), Large-scale variations in the obliquity of Mars, *Science*, 181, 260-262, doi: 10.1126/science.181.4096.260.

Warner, N.H, and J.D. Farmer (2008), Importance of aeolian processes in the origin of north polar chasmata, Mars, *Icarus*, 196, 368-384, doi: 10.1016/j.icarus.2007.08.043.

Wieczorek, M.A. (2008), Constraints on the composition of the martian south polar cap from gravity and topography, *Icarus*, 196, 506-517, doi: 10.1016/j.icarus.2007.10.026.

Zuber, M.T., R.J. Phillips, J.C. Andrews-Hanna, S.W. Asmar, A.S. Konopliv, F.G. Lemoine, J.J. Plaut, D.E. Smith, and S.E. Smrekar (2007), Density of Mars' south polar layered deposits, *Science*, 317, 1718-1719, doi: 10.1126/science.1146995.

Figure 1. (a) Location and type of the mapped discontinuities in optical images and radargrams. Analyzed stratigraphic exposures are labeled from L1 to L21; red crosses are outcrops affected by angular unconformities; white crosses are outcrops showing uncertain angular unconformities. Solid red and white lines (1-27) represent the approximated plan-view projection of subsurface angular unconformities observed in SHARAD radargrams (TO are transversal orbits). Dotted orange inset highlights the type section location (L7). Dotted white inset enclose the main area affected by radar angular unconformities (cf. Section 2). Topographic sections NS(w), NS(e) and EW (white T symbols) are referred to Fig. 15. (b) MOLA gridded topography of PL region. (c) a-a' topographic section of PL (figure b for location). The region has a maximum thickness of about 1000-1500 m (uncertainties are due to the buried bedrock elevation).

Credits: MOLA 512 pix/degree and shaded relieves.

Figure 2. a) Observed angular unconformity and mapped correlative discontinuity/conformity (AUR1; cf. Section 3.1) in section L7 (cf. Tab. 1); b, c) Narrow-scale view, not-mapped (b) and mapped (c) of the exposed angular unconformity. The white arrow indicates the dip direction of the scarp (i.e., the direction toward which the topographic elevation decreases). The torch in the upper right of images indicates the direction of illumination of the image.

Credits: a) HRSC nd3 H2169_0000; b, c) CTX P13_006290_1017, P11_005222_1021 (in (b) the image is contrast-enhanced; in (c) the image has inverted brightness.

Figure 3. a) Broad-scale location of observed angular unconformity and mapped correlative discontinuity (AUR1; cf. Section 3.1) exposed along Ultimum Chasma scarps (L18; cfr. Tab. 1). b, c) Narrow-scale view, not-mapped (b) and mapped (c) of the angular unconformity exposed in the L18 log.

Credits: CTX P12_00563_1006. Image (c) is contrast-enhanced.

Figure 4. a) Broad-scale location of observed angular unconformity and mapped correlative discontinuity (AUR1; cf. Section 3.1) exposed along Promethei Chasma scarps (L20; cfr. Tab. 1). b, c) Narrow-scale view, not-mapped (b) and mapped (c) of the angular unconformity exposed in the L20a log.

Credits: CTX B08_012710_0966. Image (b) is contrast-enhanced.

Figure 5. Subsurface angular unconformity AUR1 dividing two sets of radar bright reflectors characterized by different dipping angle, consistent with the exposed RTS and SSS sequences. Some of them are clearly truncated by the unconformable surface. The transition between the two sequences is in some cases marked by low intensity reflections zones ~100 m thick that rests upon the unconformities when present (letter A in figure). The topographic surface is located around the average MOLA elevation of ~2300 m (black and blue dashed line).

Credits: SHARAD along-track radargram, orbit rdr0938801 (cf. red line 24 in Fig. 1a and Tab. 2). Vertical depth is calculated assuming permittivity (ε) equal to 3.4 (~ice mean and dust particles).

Figure 6. a, b) Subsurface angular unconformity AUR1 dividing two set of radar reflectors characterized by different dipping, consistent with the exposed RTS and SSS sequences (a, not-mapped; b, mapped). Some of them are clearly truncated by the unconformable surface. The transition between the two sequences is in some cases marked by low intensity reflections zones ~100 m thick that rests upon the unconformities when present (letter A in figure); c) MOLA topographic cross section of the AB segment. As reference, the average elevation of the surface is around 2300 m.

Credits: SHARAD along-track radargram, orbit rdr0220201 (cf. red line 1 in Fig. 1a and Tab. 2). (b) radargram is radiometrically inverted. Vertical depth is calculated assuming permittivity (ε) equal to 3.4 (~ice mean and dust particles).

Figure 7. a, b) Subsurface angular unconformity AUR1 on radargram crosscutting orbits in figures 5 and 6 and dividing two set of radar reflectors, consistent with the exposed RTS and SSS sequences. Also in this case some radar reflectors are (with some uncertainty) characterized by different dipping angle (a, not-mapped; b, mapped); c) MOLA topographic cross section of the AB segment. As reference, the average elevation of the surface is around 2300 m.

Credits: SHARAD along-track radargram, orbit rdr0673001 (cf. white TO line 19 in Fig. 1a and Tab. 2). (b) radargram is radiometrically inverted. Vertical depth is calculated assuming permittivity (ε) equal to 3.4 (~ice mean and dust particles).

Figure 8. 3D-view of the subsurface radar AUR1 plane (cf. Fig. 1a for location and Section 2.2). The DEM shows an irregular and continuous discontinuity surface, roughly decreasing in elevation (i.e., dipping) toward SE. The DEM has been obtained from the interpolation of sample elevation points (representing the minimum, the intermediate and the maximum elevation of each radar-observed unconformity in each radargram), using Kriging method. Each point is, thus, defined by latitude, a longitude and an elevation, this latter obtained subtracting, in each radar orbit, the average elevation of the surface from the respective measured depth from the surface of the point.

Figure 9. a, b) Subsurface angular unconformity AUR1 (a, not-mapped; b, mapped) dividing two set of radar reflectors characterized by different dipping angle, consistent with the visible RTS and SSS sequences. It is located in correspondence of the type section L7b, where the AUR1 is exposed. The top sequence appears to have reflectors interrupted by the inferred unconformity; c) MOLA topographic cross section of the AB segment. As reference, the average elevation of the surface is around 2400 m.

Credits: SHARAD along-track radargram, orbit rdr0656701 (line 17 in Fig. 1a and Tab. 2). (b) radargram is radiometrically inverted. Vertical depth is calculated assuming permittivity (ε) equal to 3.4 (~ice mean and dust particles).

Figure 10. Topographic profile from MOLA gridded data of the type section (L7b) and dip-angle of the scarp. The stratigraphic boundary between the RTS and SSS sequences, coinciding with the discontinuity plane AUR1, is in some cases marked by a slight change in the topographic gradient of the profile. On the right is reported the stratigraphic section of the sequence.

Figure 11. Stratigraphic type section (L7b), not mapped (a) and mapped (b). The dashed white inbox indicates the location of Figs. 10-12. Cf. Section 2 for a detailed description of the stratigraphy.

Credits: CTX P10_005103_0995. Image (a) is contrast-enhanced.

Figure 12. Focus on type section stratigraphy (L7b). a) The discontinuity AUR1 spaces out a layered "stair-stepped" top sequence (SSS; left on the image) from a thin layered "ridge and trough" bottom sequence (RTS; right on the image). The contact between the two sequences is marked by the presence of benched layers (Bn) within the RTS; b) Detailed view of the RTS layering (Rg: ridge shaped layers, bright and convex-upward in section view; Tr: trough shaped layers, dark and concave-upward in section view; Ly is to indicate an example location of sub-metric layering, only visible at HiRISE resolution); c) Detailed view on a benched layer, showing notched edges (Ne in figure (a) as example).

Credits: HiRISE PSP_004655_1005.

Figure 13. Focus on type section stratigraphy (L7b). Detailed view of the SSS layering, mostly characterized by benched layer (Bn), in some cases showing notched edges (Ne as example).

Credits: CTX P10_005103_0995.

Figure 14. Correlation of the L7b type section (a; PL margins) with two stratigraphic exposures of

example, located in Chasma Australe (b; L5) and Ultimum Chasma (c; L18; cf. Fig. 1a for location), through the regional discontinuity AUR1, spacing out the PL1 and PL2 units. The PL1 maintains the RTS morphology in all the outcrops, but it can differ from the type section mainly in terms of thickness (several pinch-out closure of sub-sequences are inferable across the region). The PL2 is mostly characterized by benched layers (SSS morphology), but it can include also thinner "ridge and trough" layering, especially in exposures located at the borders with Ultima Lingula and Australe Lingula regions (see section c as an example). This is consistent with conventional stratigraphy on Earth (Salvador, 1987; Catuneanu, 2006), in which discontinuities are used to correlate and define discontinuity-bounded sequences irrespectively of their eventual morphological or lithological lateral changes in the depositional environment.

Figure 15. Regional stratigraphy of the SPLD sequence in PL, represented, in each figure, through logs correlation using the regional discontinuities and along three topographic profiles (from top to bottom respectively NS(w), NSe, EW; cf. Fig. 1a for logs location and Section 3 for detailed analysis). With gray-borders are represented logs obtained from radargrams. Logs with dashed borders are not located along the topographic profile but projected from locations close to it. To note the slight dip (i.e., decrease of the mean elevation) toward PL margins of the discontinuity AUR1. The elevation of the buried bedrock (i.e., the SPLD base) is not measured, but it has been obtained through interpolation from exposed outcrops around the ice-sheet. The elevation of the buried bedrock is consistent with the elevation calculated through MARSIS and SHARAD [*Plaut et al.*, 2007]. Cf. Tab. 1 and 2 for stratigraphic logs details. PL = Promethei Lingula; UL = Ultima Lingula; AL = Australe Lingula; UC = Ultimum Chasma; PC = Promethei Chasma; CA = Chasma Australe.

Figure 16. Proposed geologic scenario and chronology of the main events characterizing the SPLD in PL (the topographic profile is referred to the type section L7b). According to our analysis, the PL

region has been affected by two main depositional stages (D1 and D2 in the scheme), setting the PL1 and PL2 units, and one main erosional/not depositional stage (E1) of regional scale, removing part of the PL1 unit and modeling the unconformity AUR1. A further erosional/not depositional phase (E2) partially removed the PL2 (AUR2). Erosion likely took place mainly through wind abrasion and sublimation. During time 1 and 2, local melting of the PL ice-sheet cannot be excluded, as possibly suggested by broad “soft-sediment” deformational systems observed in some locations [*Guallini et al.*, 2012]. These events were likely forced by periodic climatic changes that in turn were driven by variations in the obliquity of the planet. Later depositional phases (D3) would have deposited the Aa2 unit, unconformable resting upon the PL2 through the AUR2 discontinuity, but involving only marginally the PL region. The attitude of the drawn layering (white or black lines) is not real and just aimed to show the possible angular unconformity between the PL1 and PL2 sequences.

Table 1. Discontinuities mapped in visible images

Log Id	Lat *(South)*	Lon *(East)*	Elevation *(km)*[a]	Length *(km)*[b]	Imagery Type[c]	Imagery Id[c]	Disc Type[d]	Disc Id	Bounded Sequences[e]	Location[f]	Cf. Fig.
L1*	82.53	91.26	1.4	n.d.	HRSC	h2169	AU?	n.d.	n.d.	CA	-
L2	85.45	97.56	2.4-2.5	5	HiRISE	PSP_004933_0945	AU?	AUR2?	Aa2/SSS	CA	-
L3*	85.20	98.16	1.5	n.d.	CTX	P10_005082_0851	AU?	n.d.	n.d.	CA	-
L4*	85.19	98.30	1.8	n.d.	CTX	P10_005082_0851	AU?	n.d.	n.d.	CA	-
L5a	84.57	99.42	1.7-2	75	CTX	P10_005082_0851	CC	AUR1	SSS/RTS	CA	-
L5b	84.36	101.30	1.7-2		CTX	P10_005082_0851	CC	AUR1	SSS/RTS	CA	-
L6	80.32	94.25	1.45	30	CTX HRSC	B06_011828_0996 h2069	AUn CC	AUR1? AUR1?	SSS?/RTS?	PL	A1a,b
L7a	79.49	100.53	1.7-2	122	CTX	P09_004708_0998	AU	AUR1	SSS/RTS	PL	-
L7b[g]	**79.31**	**102.23**	**1.7-1.8**		**CTX**	**P13_006290_1017** **P11_005222_1021**	**CC**	**AUR1**	**SSS/RTS**	**PL**	**2,11,12,13**
L7c	80.32	100.10	1.9-2.2		CTX	B05_011762_0997	CD	AUR1	SSS/RTS	PL	-
L8*	79.11	105.49	1.4	n.d.	HiRISE	PSP_004374_1005	Au?	AUL1?	n.d.	PL	-
L9a	79.14	107.47	1.6-2	53	CTX	P05_003078_0786	CC	AUR1	SSS/RTS	PL	-
L9b	79.31	108.19	1.5-1.7		CTX	P05_003078_0786	AUn CD	AUR1	SSS/RTS	PL	A1b,c
L10a	80.50	112.33	1.6-2.0	25	CTX HRSC	B12_014280_0989 h2440	AU	AUR1	SSS/RTS	PL	A2a,b
L10b	80.78	117.04	2.1-2.2	n.d	CTX	P10_005103_0995	CD	AUR1	SSS/RTS	PL	-
L11*	80.00	112.42	1.5	n.d.	CTX HRSC	P10_004826_1013 h2440	AU?	AUL1?	n.d.	PL	-
L12*	79.14	111.60	2.3	n.d.	CTX	B11_013779_1006	AU?	AUL2?	Aa2?/SSS	PL	-
L13	78.30	117.20	1.85-2.1	27	CTX	P12_005617_1011	AUn CD	AUR1	SSS/RTS	PL	A2b,c
L14*	79.15	124.45	2.2	n.d.	CTX	B09_013251_1002	AU?	AUL2?	n.d.	PL	-
L15a	79.36	132.13	1.6-1.7	70	CTX HRSC	B08_012842_1023 h2330	AU CD	AUR1	SSS/RTS	UC	A3a,b
L15b	79.20	130.48	1.6-1.7		CTX HRSC	P10_004799_0998 h2330	AU CD	AUR1	SSS/RTS	UC	A3a,b
L16*	81.30	144.0	1.4	n.d.	CTX	B07_012367_099	AU?	n.d.	n.d.	UC	-

		0				4					
L17	81.11	147.10	1.3-2.2	33	CTX	B08_012802_0983	AU CD	AUR1	SSS/RTS	UC	A3c,d
L18	80.56	150.54	1.6-2.1	92	CTX HRSC	P12_005603_1006 h2348	AU CD	AUR1	SSS/RTS	UC	3
L19[*]	82.16	163.18	1.9	n.d.	HiRISE	PSP_006288_0975	AU?	AUR1?	SSS?/RTS?	UC	-
L20a	82.28	142.50	2.1-2.2	59	CTX	B08_012710_0966	AU	AUR1	SSS/RTS	PC	4
L20b	81.52	141.80	2.1-2.2		CTX	B08_012710_0966	CD	AUR1	SSS/RTS	PC	4
L21[*]	84.00	149.25	1.6	n.d.	CTX	B08_012710_0966	AU?	n.d.	n.d.	PC	-

[*] Uncertain discontinuity

[a] Approximate elevation range (min-max)

[b] Approximate mapped length (n.d. = not determinable)

[c] Reference type image(s) and number

[d] AU = Angular Unconformity; CD = Correlative Discontinuity; CC = Correlative Conformity; n.d. = not determinable

[e] “Discontinuity-Bounded” Sequences (cf. Section 2)

[f] Geographic location of the discontinuities (PL = Promethei Lingula; CA = Chasma Australe; UC = Ultima Chasma; PC= Promethei Chasma

[g] Type Section

Table 2. Angular unconformities mapped in radargrams

Log Id[a]	Lat S *(Init)*[b]	Lat S *(End)*[b]	Lon E *(Init)*[b]	Lon E *(End)*[b]	Length *(km)*[c]	Elevation *(m)*[d]	Disc Type[e]	Disc Id	Bounded Sequences[f]	SHARAD Orbit Id[g]	Cf. Fig.
1(1)	**82.85S**	**118.80E**	**81.16S**	**114.26E**	**150**	**1700**	**AU**	**AUR1**	**SSS/RTS**	**rdr0220201**	**6**
2(1)	82.38S	116.82E	81.16S	114.26E	80	1900-2100	AU	AUR1	SSS/RTS	rdr0241301	A10
3(1)	82.66S	117.09E	81.25S	113.37E	90	1900-2000	AU	AUR1	SSS/RTS	rdr0262401	-
4(1)	82.77S	116.81E	81.22S	112.67E	98	1900-2100	AU	AUR1	SSS/RTS	rdr0283501	-
5(1)	82.99S	116.78E	81.17S	111.75E	100	1900-2100	AU	AUR1	SSS/RTS	rdr0325701	-
6(1)	**82.32S**	**111.95E**	**81.48S**	**114.09E**	**54**	**1800?**	**AU**	**AUR1**	**SSS/RTS**	**rdr0331501**	**-**
7(1)	**84.77S**	**106.81E**	**83.16S**	**114.51E**	**109**	**2300?**	**AU**	**AUR2?**	**Aa2/SSS?**	**rdr0332801**	**-**
8(1)	83.26S	117.43E	81.16S	111.41E	120	1800-2000	AU	AUR1	SSS/RTS	rdr0346801	-
9(1)	82.98S	115.84E	81.16S	110.82E	115	1850-2100	AU	AUR1	SSS/RTS	rdr0367901	A11
10(1)	82.95S	114.71E	81.55S	110.68E	91	1800-2000	AU	AUR1	SSS/RTS	rdr0410101	-
11(1)	**83.00S**	**119.84E**	**82.02S**	**122.74E**	**64**	**1800?**	**AU**	**AUR1**	**SSS/RTS**	**rdr0411901**	**-**
12(1)	**82.76S**	**113.70E**	**81.35S**	**117.42E**	**93**	**1950-2150**	**AU**	**AUR1**	**SSS/RTS**	**rdr0417201**	**-**
13(3)	**80.46S**	**151.95E**	**78.87S**	**149.46E**	**99**	**2100?**	**AU**	**AUR1**	**SSS/RTS**	**rdr0428401**	**-**
14(1)	84.27S	128.19E	81.66S	118.71E	170	1600-1900	AU	AUR1	SSS/RTS	rdr0440401	-
15(1)	**83.17S**	**115.05E**	**81.77S**	**119.17E**	**92**	**2000-2100**	**AU**	**AUR1**	**SSS/RTS**	**rdr0446201**	**A12**
16(1)	**83.05S**	**111.82E**	**81.51S**	**116.16E**	**72**	**1950-2150**	**AU**	**AUR1**	**SSS/RTS**	**rdr0459401**	**-**
17(2)	81.63S	104.81E	79.92S	101.32E	107	1700-2250	AUn	AUR1	SSS/RTS	rdr0656701	12
18(1)	**82.88S**	**113.80E**	**81.61S**	**117.31E**	**81**	**2000**	**AU**	**AUR1**	**SSS/RTS**	**rdr0658501**	**-**
19(1)	**83.00S**	**114.32E**	**81.60S**	**118.28E**	**91**	**2000-2100**	**AU**	**AUR1**	**SSS/RTS**	**rdr0673001**	**7**
20(1)	**82.61S**	**112.39E**	**81.35S**	**115.69E**	**81**	**1800-2000**	**AU**	**AUR1**	**SSS/RTS**	**rdr0700701**	**-**
21(1)	**82.49S**	**110.67E**	**80.94S**	**114.48E**	**98**	**1800?**	**AU**	**AUR1**	**SSS/RTS**	**rdr0707301**	**-**
22(1)	83.26S	122.00E	81.74S	117.27E	98	1700	AU	AUR1	SSS/RTS	rdr0896601	-
23(1)	82.43S	119.67E	81.16S	116.42E	130	1750	AU	AUR1	SSS/RTS	rdr0932201	-
24(1)	82.42S	117.86E	81.46S	115.17E	100	1800-1900	AU	AUR1	SSS/RTS	rdr0938801	5
25(2)	81.56S	104.04E	79.99S	100.82E	98	1700-2250	AU	AUR1	SSS/RTS	rdr1056201	-
26(1)	**82.96S**	**114.90E**	**81.70S**	**118.44E**	**115**	**2000-2100**	**AU**	**AUR1**	**SSS/RTS**	**rdr1610501**	**-**
27(1)	83.85S	125.57E	81.77S	118.62E	180	1600-2100	AU	AUR1	SSS/RTS	rdr1640301	-
28(2)	**83.01S**	**102.35E**	**81.18S**	**107.27E**	**81**	**1800-1900**	**AU**	**AUR1**	**SSS/RTS**	**rdr1614501**	**-**

Bold rows are transversal orbits crossing longitudinal orbits.

[a] Numbers identify single observed unconformities. In parenthesis are reported the identification numbers of orbits displaying the angular unconformity in the same location.

[b] Approximate beginning and end of the unconformities, projected on surface in plan-view (cf. Fig. 1a)

[c] Approximate mapped length

[d] Approximate elevation range (min-max)

[e] AU = Angular Unconformity

[f] "Discontinuity-Bounded" Sequences (cf. Section 2)

[g] SHARAD reference orbit

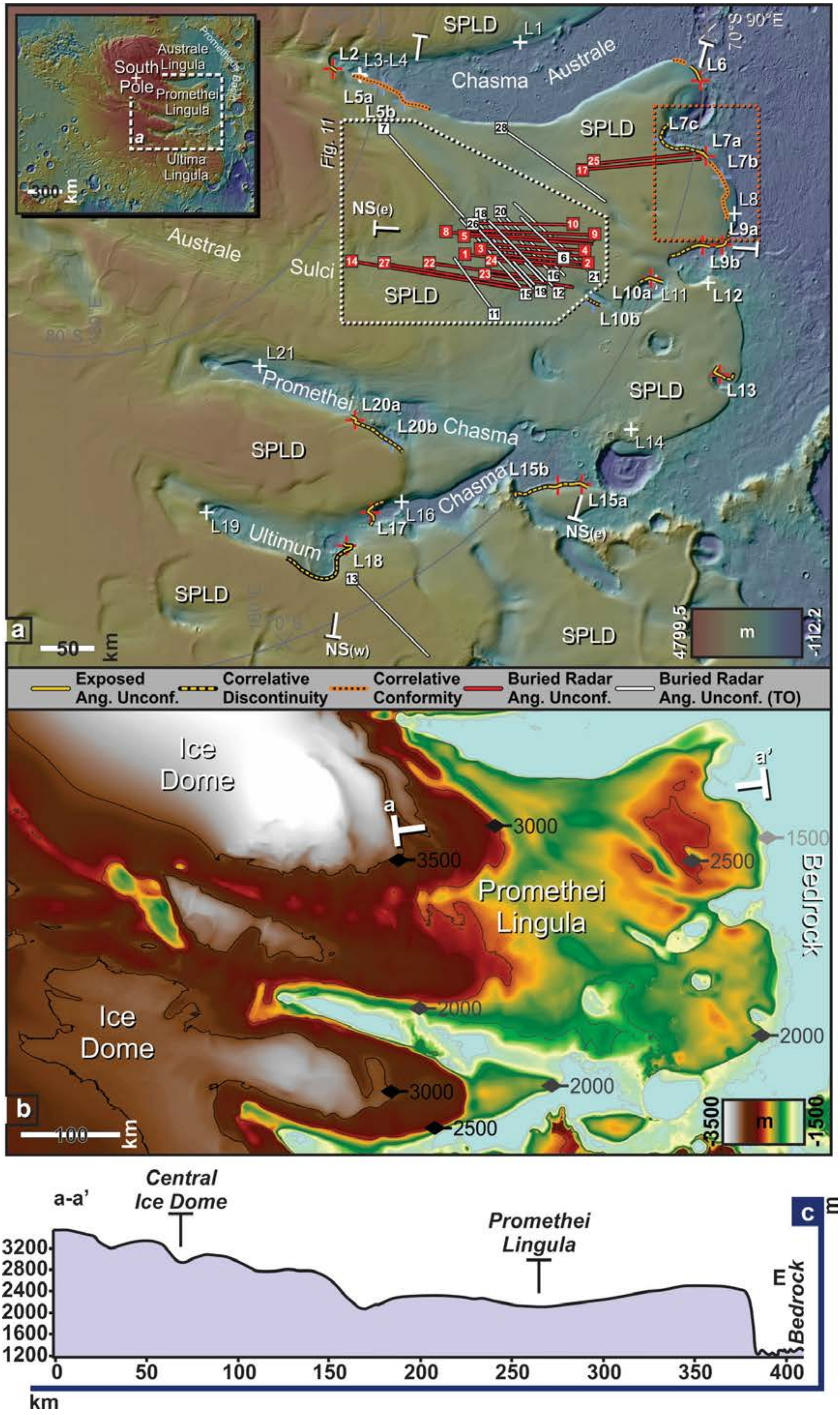
a
South Pole
Australe Lingula
Promethei Lingula
Ultima Lingula
Promethei Basin
300 km
SPLD
L1
L2
L3-L4
L5a
L5b
L6
L7a
L7b
L7c
L8
L9a
L9b
L10a
L10b
L11
L12
L13
L14
L15a
L15b
L16
L17
L18
L19
L20a
L20b
L21
Australe Chasma
Australe Sulci
Promethei Chasma
Ultimum Chasma
Fig. 11
NS(e)
NS(w)
70°S 90°E
80°S
50 km
4799.5
m
-112.2
Exposed Ang. Unconf.
Correlative Discontinuity
Correlative Conformity
Buried Radar Ang. Unconf.
Buried Radar Ang. Unconf. (TO)
b
Ice Dome
Ice Dome
Promethei Lingula
Bedrock
a
a'
3500
3000
2500
2000
1500
100 km
-3500
m
-1500
c
a-a'
Central Ice Dome
Promethei Lingula
Bedrock
m
3200
2800
2400
2000
1600
1200
0
50
100
150
200
250
300
350
400
km

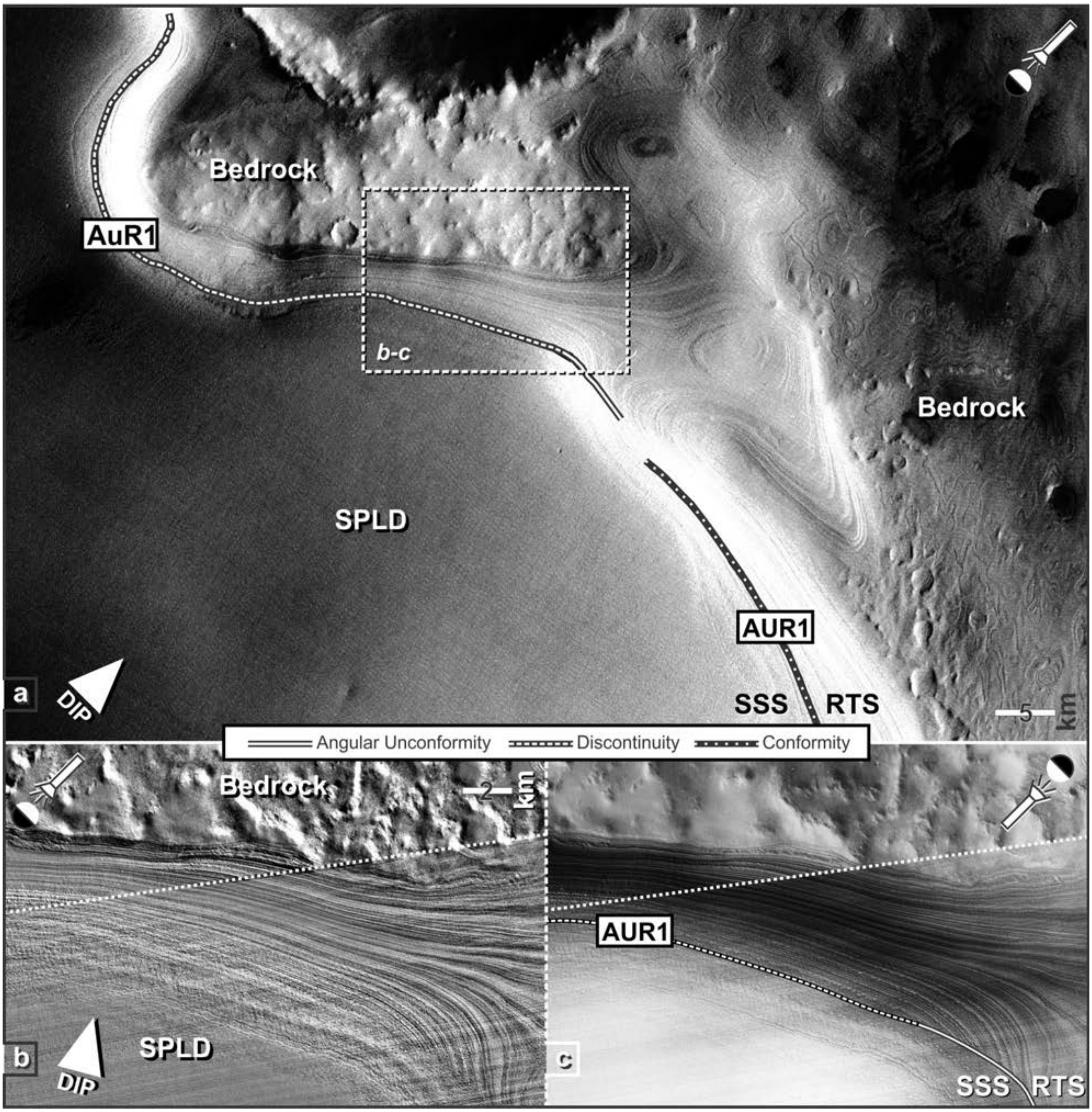
Bedrock
AuR1
b-c
Bedrock
SPLD
AUR1
a
DIP
SSS
RTS
5 km
Angular Unconformity
Discontinuity
Conformity
Bedrock
2 km
b
DIP
SPLD
AUR1
c
SSS
RTS

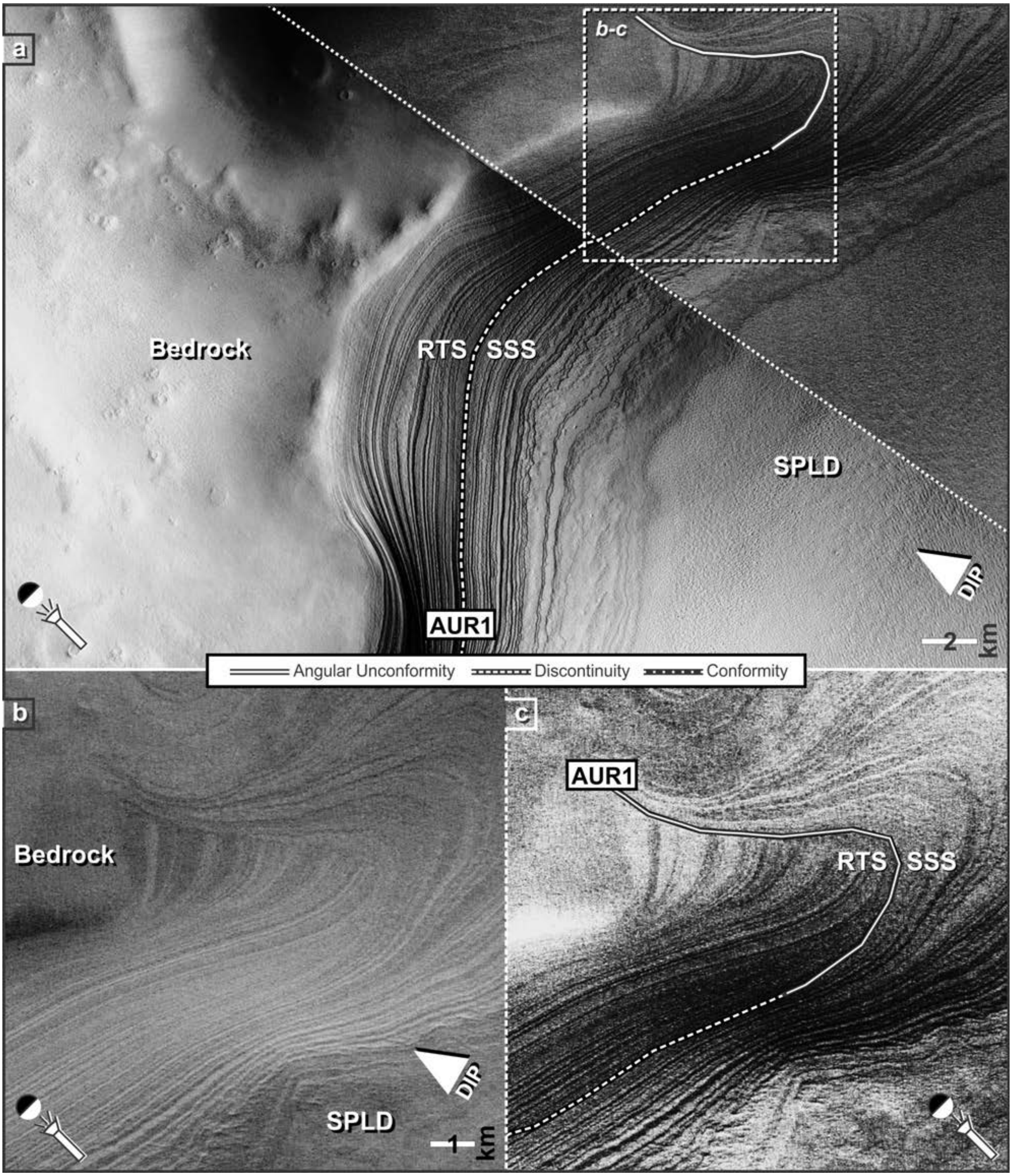
a
b-c
Bedrock
RTS
SSS
SPLD
DIP
2 km
AUR1
Angular Unconformity
Discontinuity
Conformity
b
Bedrock
DIP
SPLD
1 km
c
AUR1
RTS
SSS

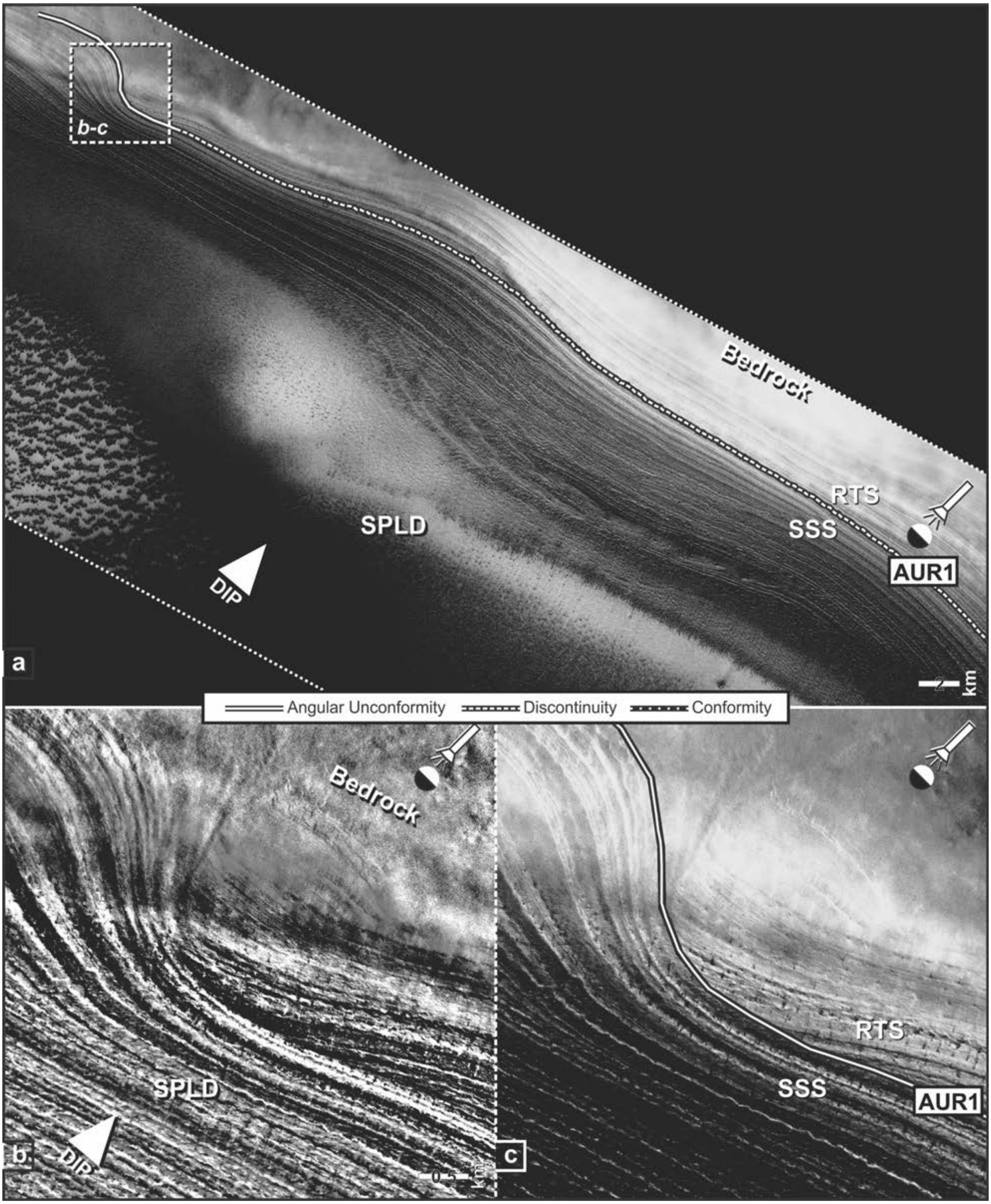
b-c
Bedrock
RTS
SSS
AUR1
SPLD
DIP
a
2 km
Angular Unconformity
Discontinuity
Conformity
Bedrock
SPLD
DIP
b
0.5 km
c
RTS
SSS
AUR1

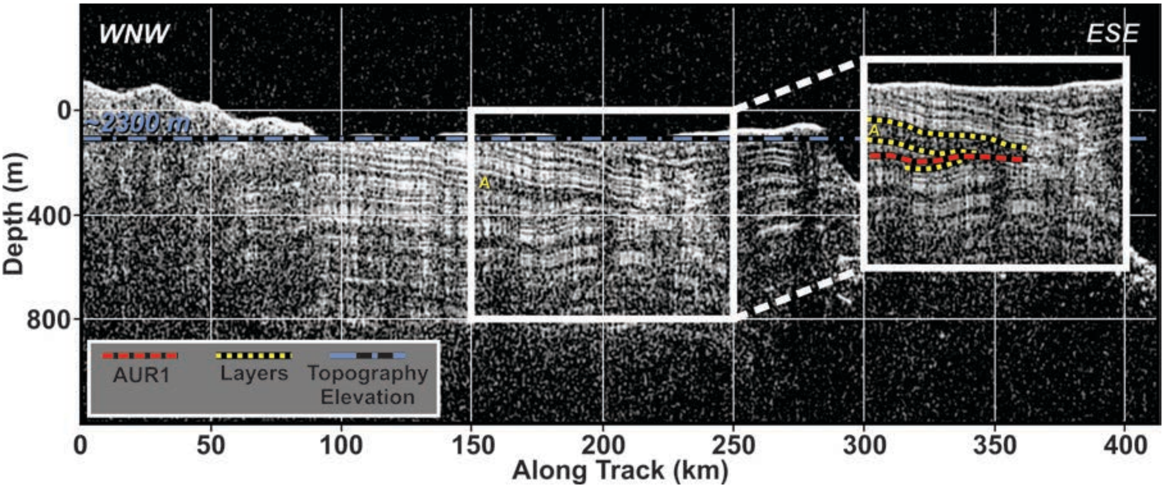
WNW
ESE
~2300 m
A
A
Depth (m)
0
400
800
AUR1
Layers
Topography Elevation
0
50
100
150
200
250
300
350
400
Along Track (km)

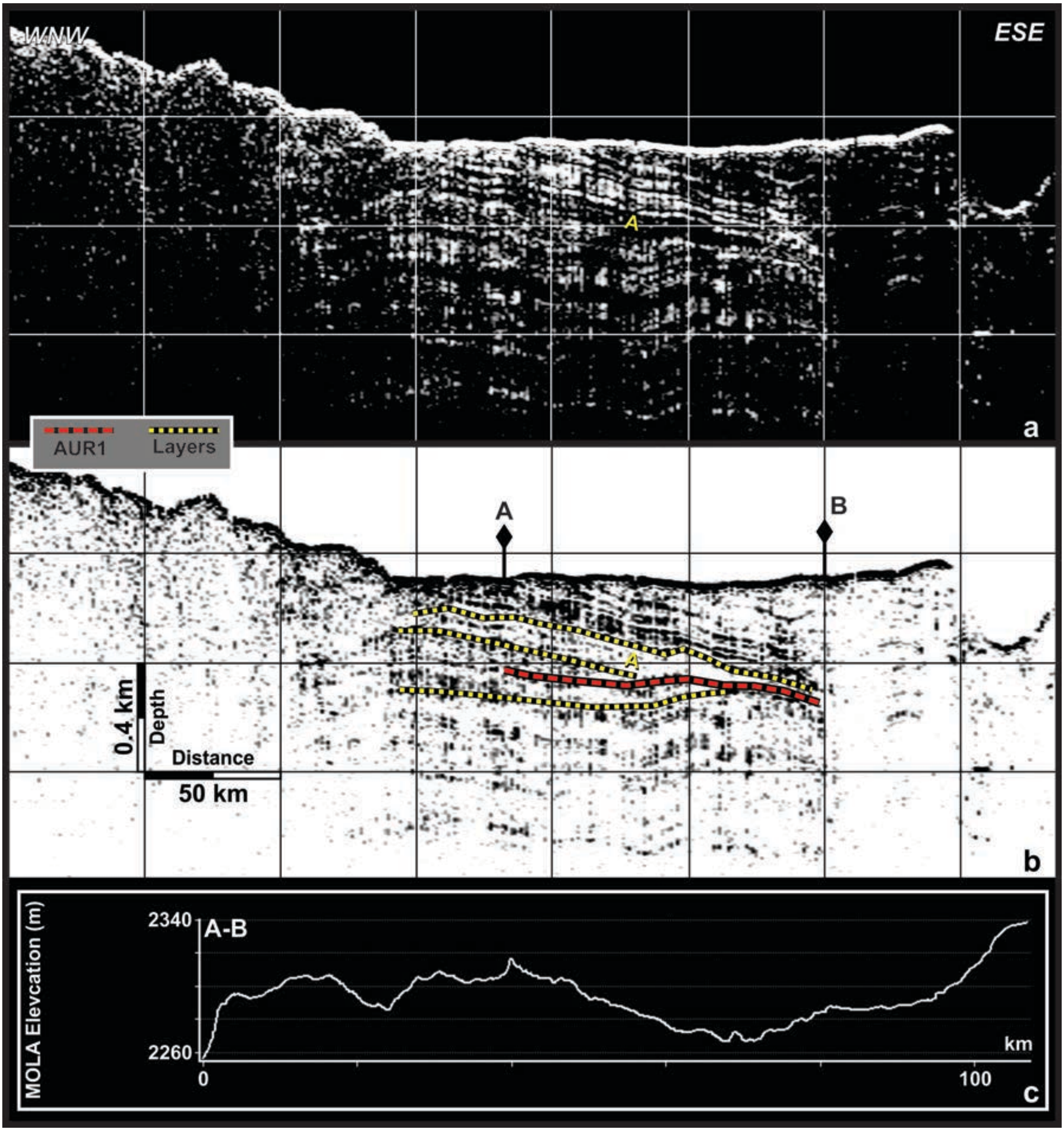
WNW
ESE
A
a
AUR1
Layers
A
B
A
0.4 km
Depth
Distance
50 km
b
MOLA Elevcation (m)
2340
A-B
2260
km
0
100
c

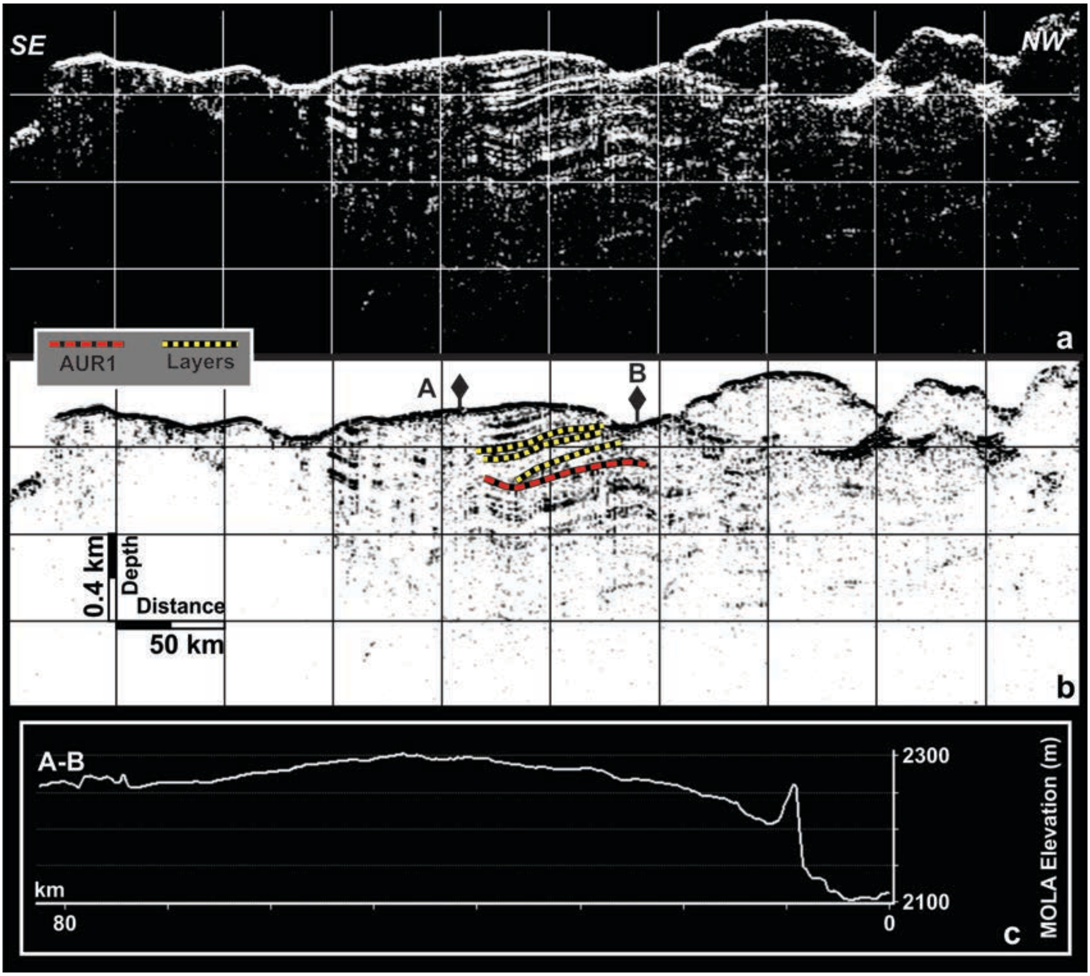
SE
NW
a
AUR1
Layers
A
B
0.4 km
Depth
Distance
50 km
b
A-B
2300
2100
MOLA Elevation (m)
km
80
0
c

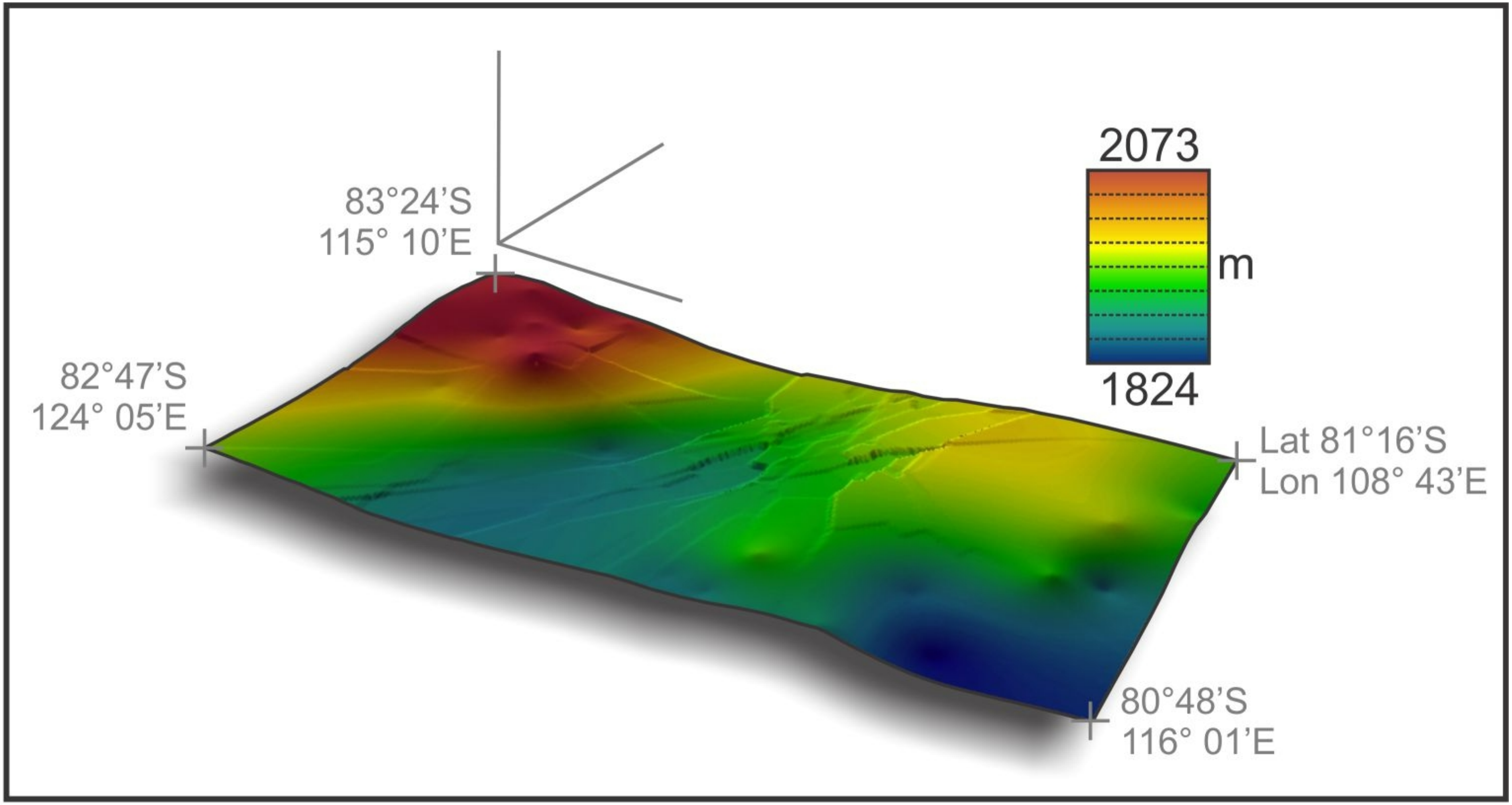
83°24'S
115° 10'E
82°47'S
124° 05'E
2073
m
1824
Lat 81°16'S
Lon 108° 43'E
80°48'S
116° 01'E

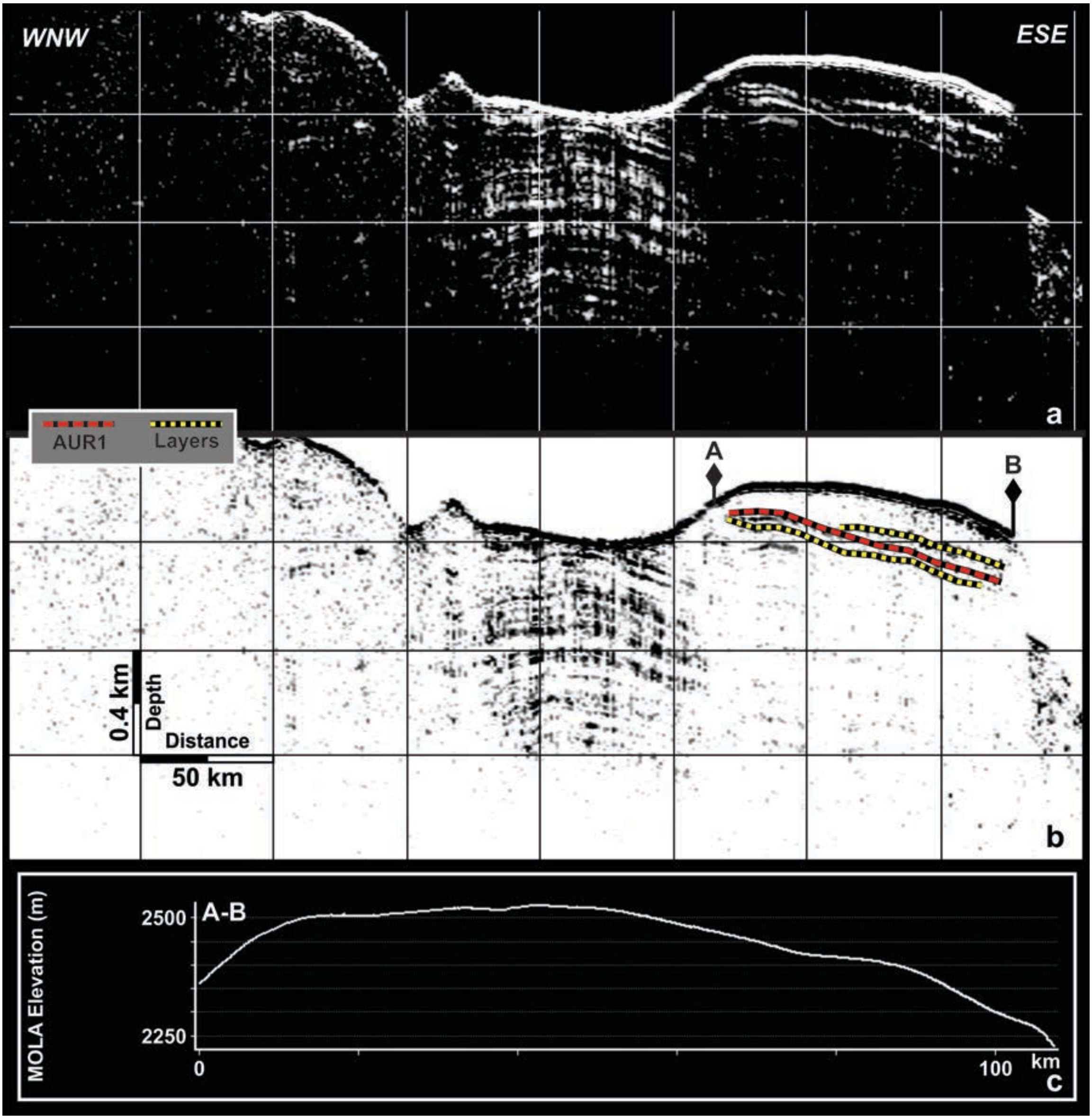
WNW
ESE
a
AUR1
Layers
A
B
0.4 km
Depth
Distance
50 km
b
MOLA Elevation (m)
2500
2250
A-B
0
100
km
c

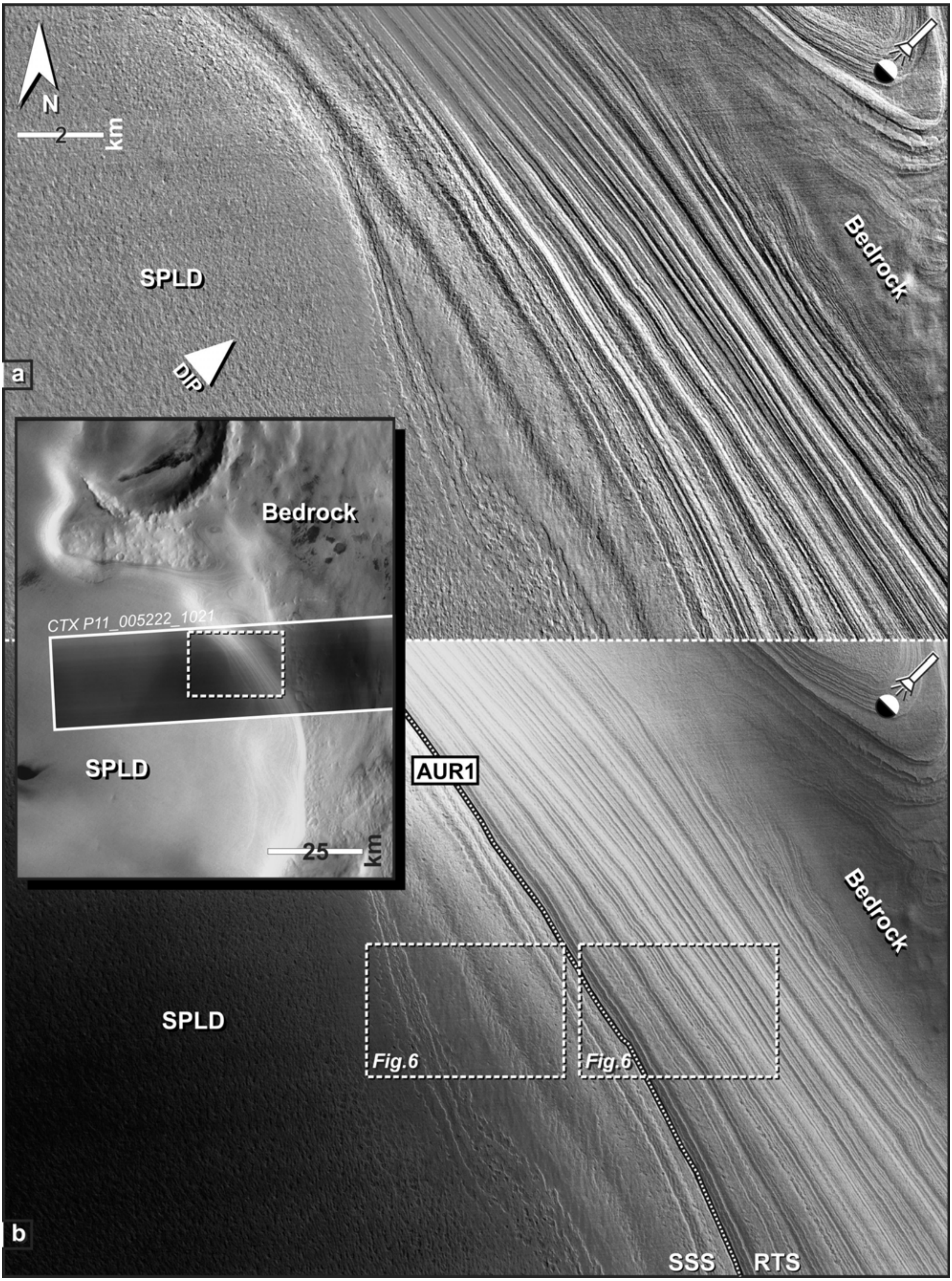
N
2 km
SPLD
Bedrock
DIP
a
Bedrock
CTX P11_005222_1021
SPLD
25 km
AUR1
Bedrock
Fig.6
Fig.6
SPLD
b
SSS
RTS

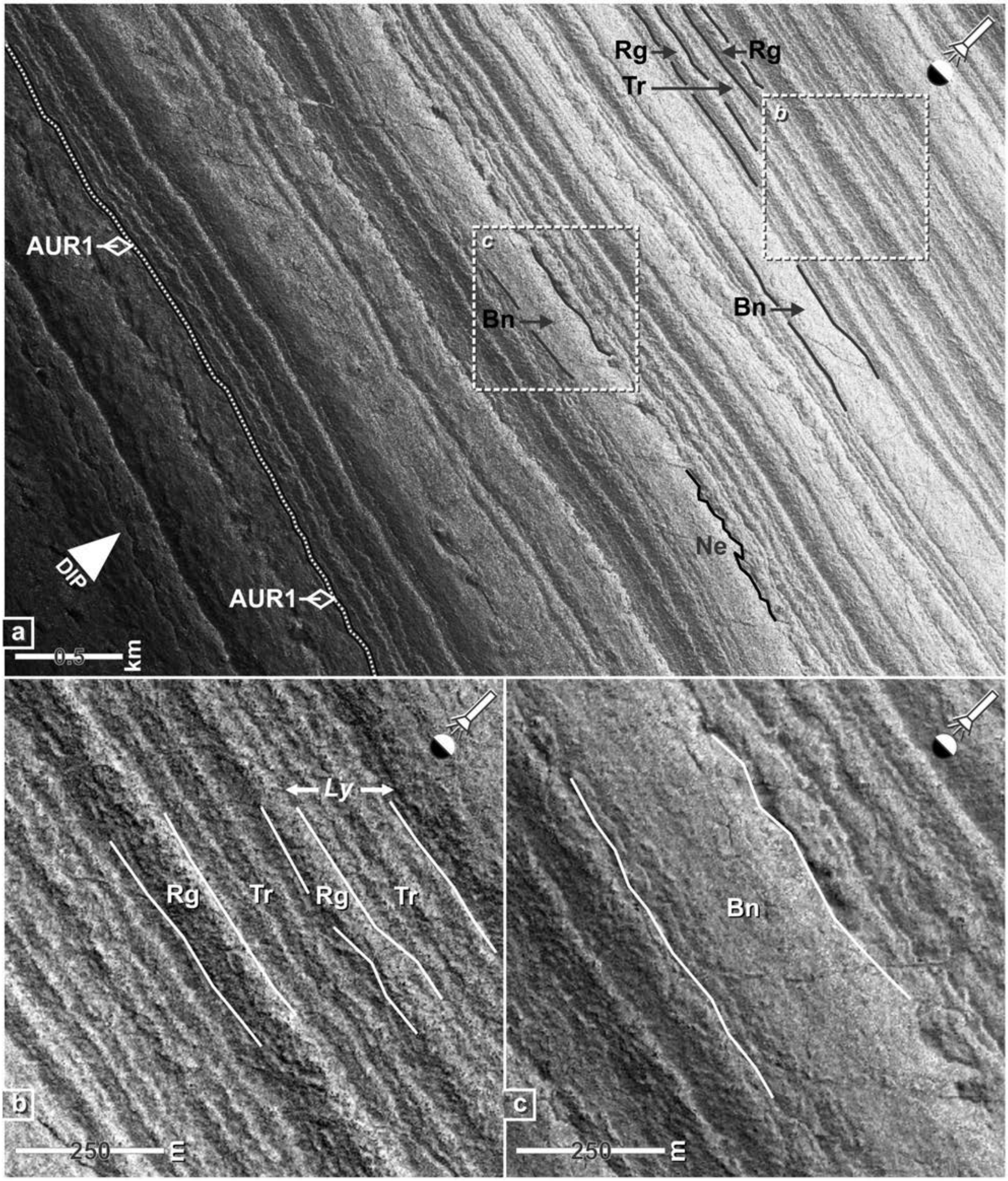
Rg
Rg
Tr
b
AUR1
c
Bn
Bn
Ne
DIP
AUR1
a
0.5 km
Ly
Rg
Tr
Rg
Tr
b
250 m
Bn
c
250 m

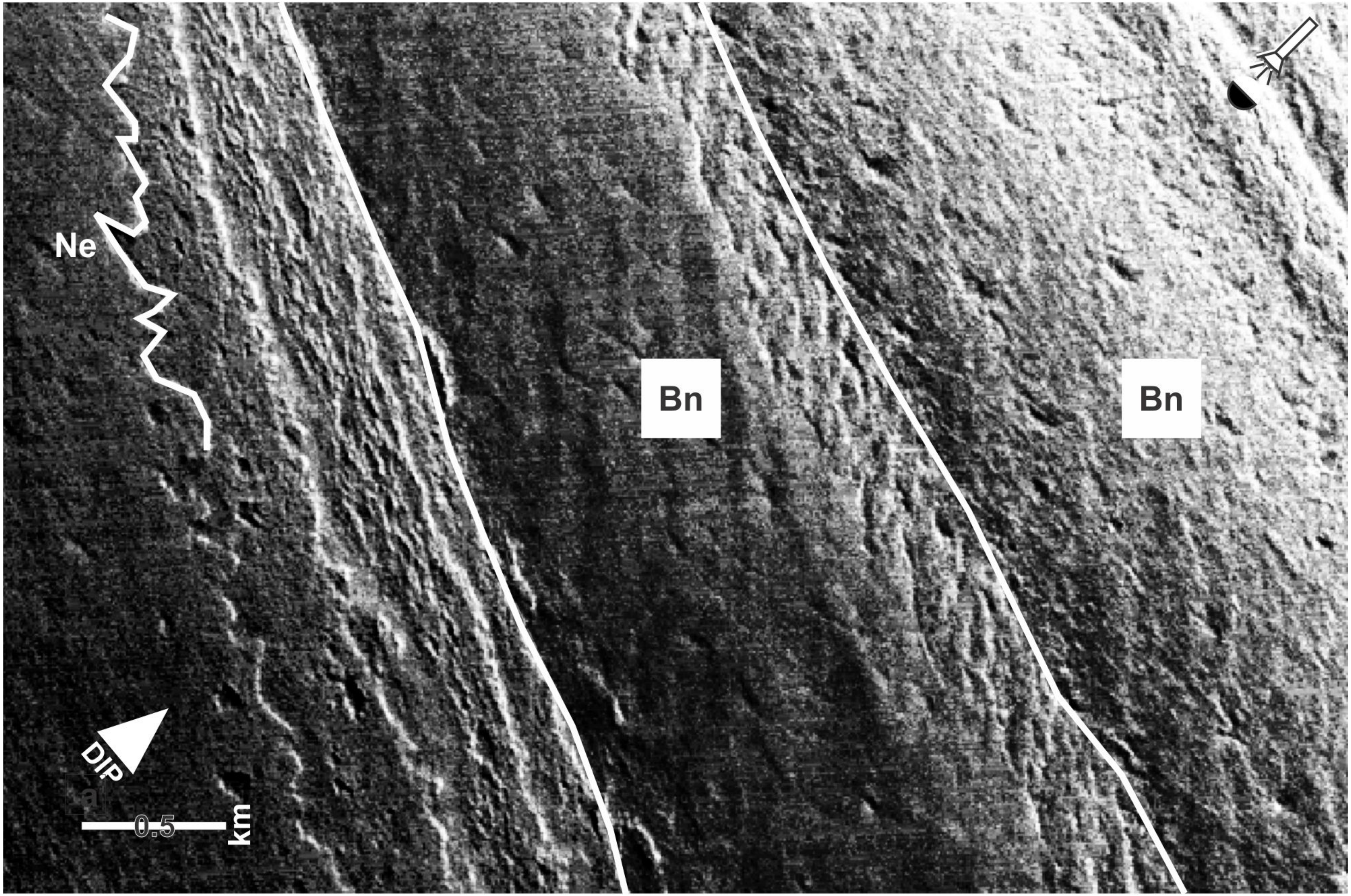
Ne
Bn
Bn
DIP
a
0.5
km

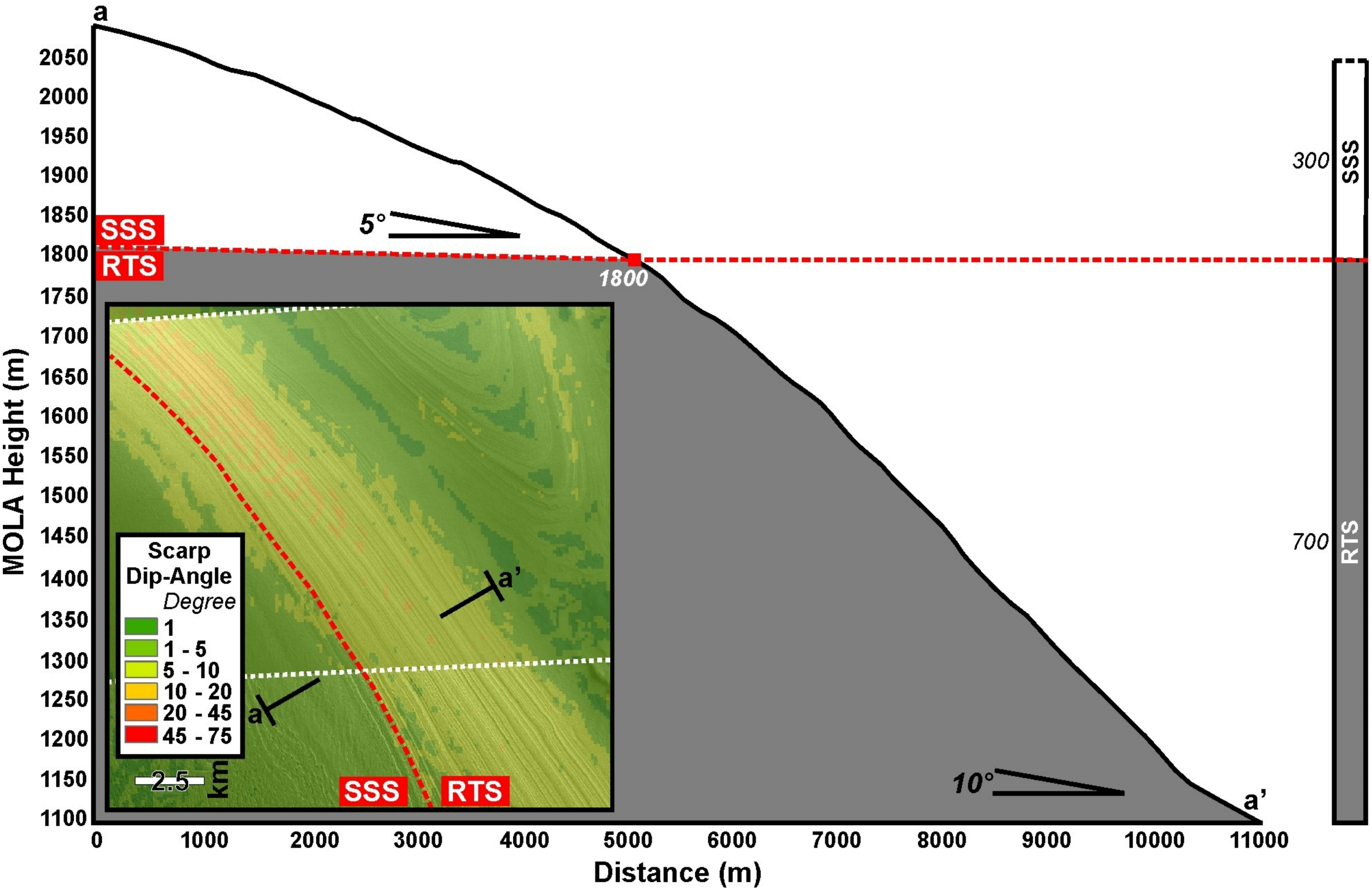
a
a'
MOLA Height (m)
2050
2000
1950
1900
1850
1800
1750
1700
1650
1600
1550
1500
1450
1400
1350
1300
1250
1200
1150
1100
0
1000
2000
3000
4000
5000
6000
7000
8000
9000
10000
11000
Distance (m)
SSS
RTS
5°
10°
1800
300
SSS
700
RTS
Scarp
Dip-Angle
Degree
1
1 - 5
5 - 10
10 - 20
20 - 45
45 - 75
2.5
km
a
a'
SSS
RTS

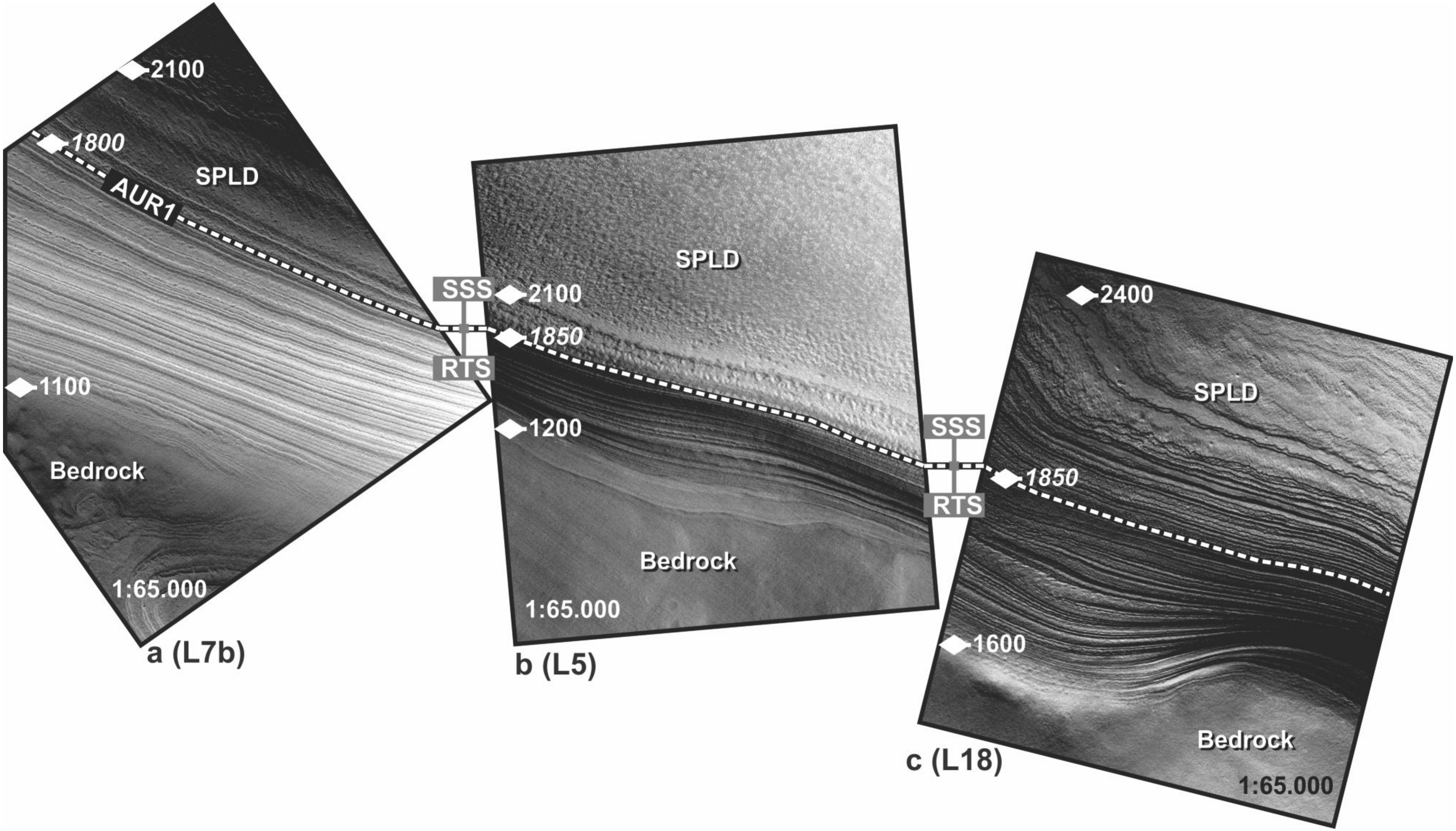
2100
1800
AUR1
SPLD
1100
Bedrock
1:65.000
a (L7b)
SSS
RTS
2100
1850
SPLD
1200
Bedrock
1:65.000
b (L5)
SSS
RTS
2400
SPLD
1850
1600
Bedrock
1:65.000
c (L18)

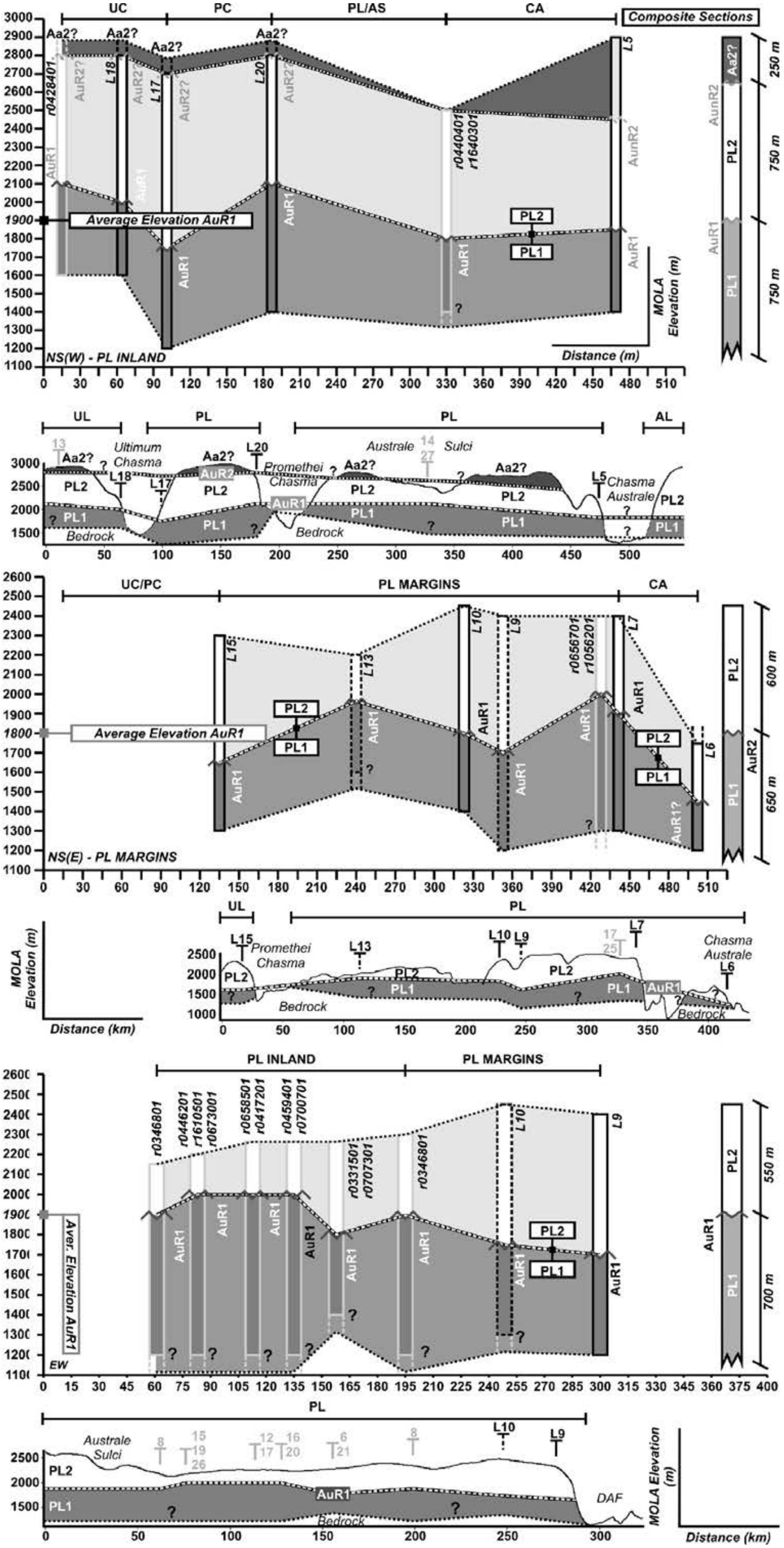
UC
PC
PL/AS
CA
Composite Sections
Aa2?
AuR2?
AuR1
AunR2
PL2
PL1
250 m
750 m
750 m
r0428401
L18
L17
L20
L5
r0440401
r1640301
Average Elevation AuR1
MOLA Elevation (m)
Distance (m)
NS(W) - PL INLAND
UL
PL
AL
Ultimum Chasma
Promethei Chasma
Australe Sulci
Chasma Australe
Bedrock
UC/PC
PL MARGINS
L15
L13
L10
L9
r0656701
r1056201
L7
L6
AuR1?
600 m
650 m
NS(E) - PL MARGINS
Distance (km)
PL INLAND
r0346801
r0446201
r1610501
r0673001
r0658501
r0417201
r0459401
r0700701
r0331501
r0707301
Aver. Elevation AuR1
EW
550 m
700 m
DAF
MOLA Elevation (m)

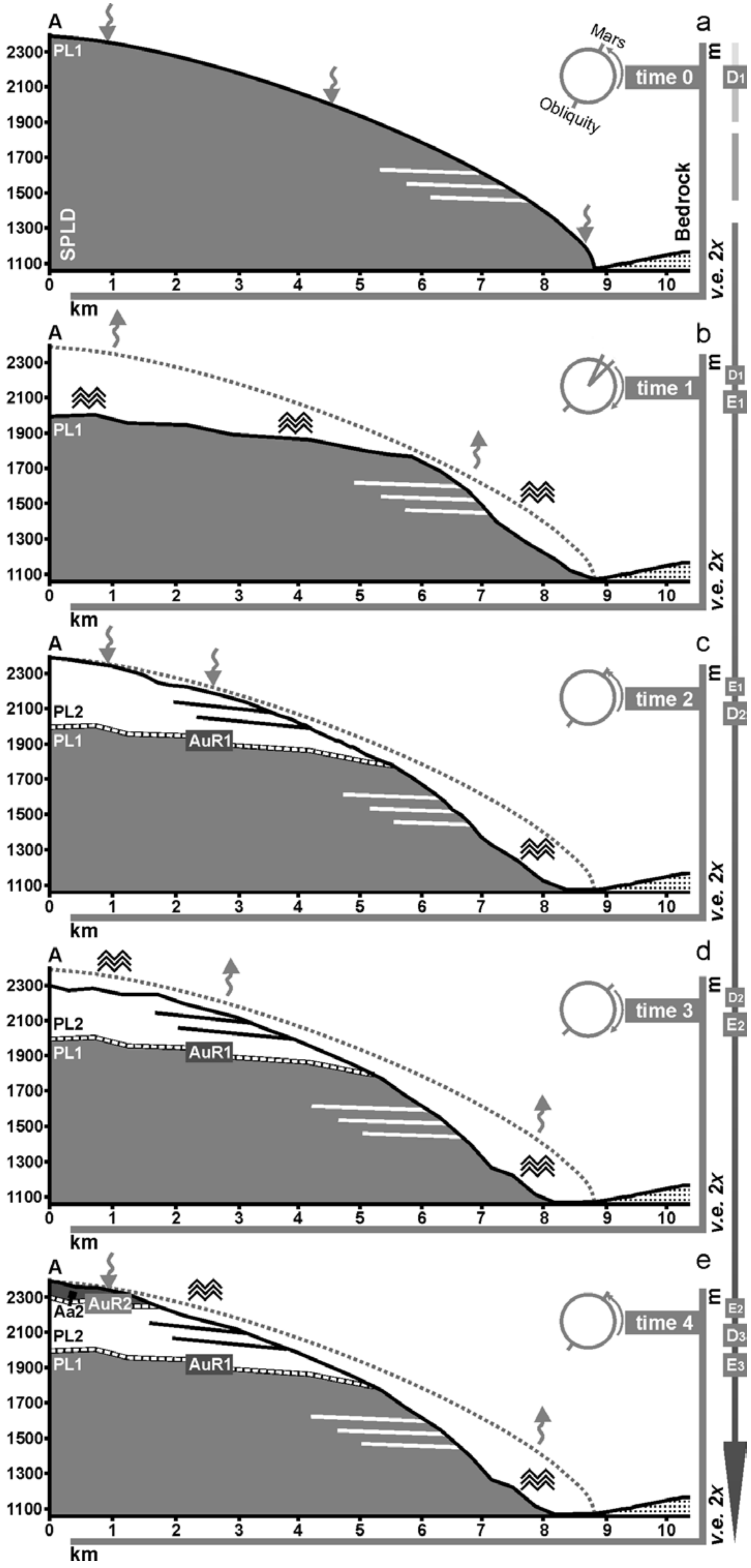
a
b
c
d
e
A
PL1
PL2
SPLD
Bedrock
AuR1
AuR2
Aa2
Mars
Obliquity
time 0
time 1
time 2
time 3
time 4
D1
E1
D2
E2
D3
E3
m
km
v.e. 2x
2300
2100
1900
1700
1500
1300
1100
0
1
2
3
4
5
6
7
8
9
10